



A novel nanocomposite based on sodalite and green copper nanoparticles: In vitro safety profile, ecotoxicity and deep learning study for photodegradation of a binary mixture of dyes

Leandro Rodrigues Oviedo ^a, Daniel Moro Druzian ^a, Sth  fany Nunes Loureiro ^a, Alencar Kolinski Machado ^b, Ta  se Regina Schuster Montagner ^b, Giovani Pavoski ^c, Denise Crocce Romano Espinosa ^c, Yolice Patricia Moreno Ruiz ^d, Lissandro Dorneles Dalla Nora ^a, William Leonardo da Silva ^{a,*}

^a Applied Nanomaterials Research Group (GPNAp), Franciscan University (UFN), Santa Maria, RS, Brazil

^b Laboratory of Cell Culture and Bioactive Effects, Franciscan University (UFN), Santa Maria, RS, Brazil

^c Polytechnical School of Chemical Engineering, University of the Sao Paulo (USP), S  o Paulo, SP, Brazil

^d Department of Fundamental Chemistry (DQF), Federal University of Pernambuco (UFPE), Recife, PE, Brazil

ARTICLE INFO

Keywords:

Heterogeneous photocatalysis

Green synthesis

Artificial neural networks

ABSTRACT

This work aims to develop an eco-friendly nanocomposite (nSOD@CuO-NPs) for the photodegradation of a binary dye mixture of crystal violet (CV) and methylene blue (MB). nSOD@CuO-NPs was constituted of copper oxide nanoparticles (CuO-NPs) as the reinforcement and sodalite nanozeolite (nSOD) as the matrix. CuO-NPs, nSOD, and nSOD@CuO-NPs were synthesized by green synthesis (from *Camellia sinensis* extract), hydrothermal (from agro-industrial waste), and impregnation methods. nSOD@CuO-NPs showed a mesoporous structure with analcime/sodalite and cuprite/tenorite crystalline phases, pH_{ZCP} 7.65, $ZP = -18.5 \pm 1.0$ mV, $E_g = 1.38$ eV, $S_{BET} = 14.8 \text{ m}^2 \text{ g}^{-1}$, $V_p = 0.04 \text{ cm}^3 \text{ g}^{-1}$, $d_p = 16.7 \text{ nm}$, $D_p = 20.2 \pm 14.21 \text{ nm}$. Under ideal conditions ($\text{pH } 10$, $[\text{nSOD@CuO-NPs}] = 1.5 \text{ g L}^{-1}$, and $[\text{CV: MB}] = 70 \text{ mg L}^{-1}$), nSOD@CuO-NPs achieved 79.4% degradation ($k = 0.0081 \text{ min}^{-1}$) for CV and 82.9% degradation ($k = 0.0118 \text{ min}^{-1}$) for MB after 180 min. Deep learning showed high performance (neural network (NN) architecture = 20: 15: 18: 1 | $R^2 \sim 0.915$ | RMSE ~ 0.074), predicting $\sim 85\%$ dye degradation after 240 min. In vitro safety profile revealed that nSOD@CuO-NPs preserved cellular viability, reduced ROS generation, and DNA damage in VERO cells after 72 h. Regarding ecotoxicity, nSOD@CuO-NPs showed reduced acute toxicity toward *A. salina* after 72 h compared to CuO-NPs.

1. Introduction

Approximately 50,000 tons of synthetic organic dyes are produced annually and discharged into wastewater by the textile, pulp, wool, and cellulose industries [1]. These dyes are hydrophilic, chemically and thermally stable, and resistant to physicochemical and biological wastewater treatment, posing a serious threat to aquatic life and the environment [2].

Heterogeneous photocatalysis attracts significant attention for efficiently degrading organic dyes. This process generates highly reactive oxygen species (i.e., $\text{HO}\cdot$ and $\bullet\text{O}_2^-$), which react non-selectively with organic matter, leading to its mineralization into CO_2 and H_2O [3]. This sustainable, versatile, and simple technique provides high removal

efficiencies for dyes in aqueous solutions [4].

Copper oxide nanoparticles (CuO-NPs) are promising nanocatalysts due to their low toxicity, band gap energy (E_g) between 1.2 and 1.7 eV, ferrimagnetic behavior, and ionic character. Additionally, they can be synthesized through green methods using plant extracts as reducing agents [5]. For instance, the green synthesis of CuO-NPs from green tea (*Camellia sinensis*) extract offers advantages over conventional chemical routes, such as lower toxicity, shorter reaction times, and milder synthesis conditions, while maintaining sustainability [6]. Rich in polyphenols, flavonoids, and other bioactive compounds, the extract reduces copper ions (Cu^+ and Cu^{2+}) to form CuO-NPs and stabilizes them to ensure uniform particle size and prevent agglomeration [7]. Additionally, these bioactive compounds help stabilize the nanoparticles,

* Corresponding author.

E-mail address: [williamleonardo_silva@hotmail.com](mailto:wiliamleonardo_silva@hotmail.com) (W.L. da Silva).

ensuring uniform size distribution and preventing agglomeration [8].

Nanozeolites are crystalline aluminosilicate minerals characterized by their tailored particle size, morphology, porous structure, and high surface area. Their three-dimensional frameworks consist of silicon (Si) and aluminum (Al) tetrahedra linked by oxygen atoms, forming pores that enable selective adsorption based on molecule size and shape [9,10]. Synthesizing nanozeolites (e.g., sodalite – nSOD, analcime – nANA, faujasite – nFAU) from (agro)industrial waste materials (e.g., rice husk and alum sludge) offers a sustainable and cost-effective approach, reducing waste and producing valuable nanomaterials [11,12].

In this scenario, dispersing CuO-NPs onto catalytic supports enhances photocatalytic activity by lowering band gap energy, preventing agglomeration, improving stability, and facilitating catalyst recovery. [13]. Thus, the incorporation of nanozeolites as catalytic supports further enhances CuO nanoparticles dispersion, effectively enhancing charge separation and minimizing recombination rates, ultimately leading to higher degradation efficiency [14].

In this way, CuO-NPs supported onto nanozeolites (nanozeolite@CuO-NPs) have been recognized as an efficient photocatalyst for cationic dye degradation under visible light, achieving 90–95% degradation of dyes such as methylene blue (MB), rhodamine B (RhB), and crystal violet (CV). Furthermore, some studies have reported that nanozeolite@CuO-NPs exhibit enhanced photocatalytic performance, achieving up to 85% degradation of methyl orange within 120 min [15]. However, nanocatalysts where both CuO-NPs and nanozeolite supports are synthesized using green methods are uncommon. Therefore, this work presents a novel nSOD@CuO-NPs nanocatalyst, wherein the CuO-NPs were synthesized through green synthesis and the nanozeolite was produced from waste materials, which is an uncommon combination that is scarcely found in the current literature. In this view, although CuO supported on nanozeolite has been previously documented, those materials are generally prepared via conventional chemical routes, rendering the approach used here both sustainable and innovative in the context of photocatalysis.

Although nanozeolite@CuO-NPs nanocatalysts are efficient, their experimental preparation can be time-consuming and costly. Computational approaches (e.g., machine learning – ML and deep learning – DL), can be employed to optimize photocatalytic process conditions and identify key variables influencing wastewater treatment, enabling further predictive modeling [16]. In this context, supervised machine and deep learning algorithms, including decision tree-based models (e.g., Extreme Gradient Boosting – XGB and Random Forest – RF) and neural networks (e.g., Multilayer Perceptron Artificial Neural Networks – MLP-ANN), can be used as powerful tools for predicting dye mineralization rates and identifying key degradation products [17]. Additionally, neural networks can extrapolate values beyond the experimental range, allowing for accurate predictions of kinetic curves and degradation profiles over time [18].

In this context, this study aims to develop and apply a ceramic nanocomposite consisting of sodalite (matrix) and copper oxide nanoparticles (reinforcement) for photodegradation of a binary dye mixture containing crystal violet (CV) and methylene blue (MB), integrating experimental design and deep learning methods. The experimental design was employed to determine the ideal conditions for dye degradation, while deep learning was employed to identify influential variables in the process and predict absorbance over time at three wavelengths ($\lambda = 590, 630$, and 663 nm). Furthermore, to evaluate the *in vitro* safety profile (in VERO cells) to verify the biocompatibility of the nanocomposite through cell viability/proliferation assay, and its acute toxicity in *Artemia salina*.

This work presents a ceramic nanocomposite of sodalite nanozeolite and copper oxide nanoparticles, both synthesized by green methods using industrial and agro-industrial wastes. While CuO-NPs support on nanozeolites has been reported, this study uniquely applies sustainable synthesis to both components, promoting environmental friendliness and resource valorization. Additionally, the experimental design (CCRD

2^3) optimized degradation conditions, while deep learning predicted dye absorbance over extended periods (0 to 240 min) at three wavelengths ($\lambda = 590, 630$, and 663 nm). This enabled assessment of whether the nanocatalyst activity peaks within the 180-min experimental window or continues beyond. Finally, biocompatibility and acute toxicity assays confirmed the nanocomposite's safety for environmental applications.

2. Materials and methods

2.1. Pre-treatment of waste

Alum sludge from a wastewater treatment plant was used to extract alumina (Al_2O_3), whereas rice husks were obtained from a grain processing industry located in Santa Maria (Brazil) and were chemically and thermally treated to extract silica (SiO_2), according to the literature [19,20]. Thus, 10 g of alum sludge were calcinated at 400°C for 2 h. Regarding the SiO_2 extraction, 10 g of rice husks were leached with 200 mL of HCl 2 mol L^{-1} (ACS reagent, 37%, Sigma-Aldrich®) at 60°C for 30 min, followed by calcination at 600°C for 6 h at $30^\circ\text{C min}^{-1}$.

2.2. Synthesis and characterization of the ceramic nanocomposite

A matrix constituted of sodalite nanozeolite (nSOD) was synthesized by the hydrothermal method ($180 \pm 2^\circ\text{C} / 6 \text{ h} / 5^\circ\text{C min}^{-1}$). Thus, 0.643 g of SiO_2 (treated rice husks) and 2.15 g Al_2O_3 (treated alum sludge) were dissolved in 60 mL of 2 mol L^{-1} NaOH (99%, Synth®) under magnetic stirring (120 rpm / $40 \pm 5^\circ\text{C}$) for 20 min [21]. Subsequently, the mixture was transferred to a polytetrafluoroethylene (PTFE)-lined stainless steel reactor heated at 180°C for 600 min, followed by washing (ethyl alcohol 70% with distilled water) and drying ($80^\circ\text{C} / 240$ min).

The nanoreinforcement (copper oxide nanoparticles - CuO-NPs) was synthesized by the biosynthesis from green tea leaves (*Camellia sinensis*). Thus, 20 g of ground leaves were mixed with 50 mL distilled water (extract) and 50 mL of 0.8 mol L^{-1} $\text{CuCl}_2 \cdot 2\text{H}_2\text{O}$ (analytical grade $\geq 97\%$, Sigma-Aldrich®) for 40 min under magnetic stirring (200 rpm) at $50 \pm 2^\circ\text{C}$, followed by centrifugation (4500 rpm / 10 min), drying ($80 \pm 2^\circ\text{C} / 12$ h), and calcination ($450 \pm 2^\circ\text{C} / 6 \text{ h} / 30^\circ\text{C min}^{-1}$) [22].

The ceramic nanocomposite (nSOD@CuO-NPs nanocatalyst) was prepared by impregnation [23], where the catalytic support (nSOD) was mixed with 2.5 wt% of the photoactive phase (CuO-NPs) under magnetic stirring (100 rpm / 90 min). After, the sample was dried ($80 \pm 2^\circ\text{C}$) for 3 h and calcined ($450 \pm 2^\circ\text{C}$ for 4 h). Fig. 1 shows an illustration of the nSOD@CuO-NPs synthesis.

2.3. Central composite rotational design (CCRD)

To determine the ideal condition of the heterogeneous photocatalysis under visible radiation, a Central Composite Rotational Design with three factors and two levels (CCRD 2^3) based on previous work was carried out [24]. Table 1 shows the variables and range used in the experimental design.

According to Table 1, the dye mixture concentration ([CV:MB]), nanocatalyst concentration ([nSOD@CuO-NPs]) and pH were selected as independent variables, whereas the dye degradation percentage (%R) was selected as the dependent variable. The experimental set constructed by the CCRD 2^3 resulted in 17 experiments carried out in duplicate.

2.4. Photocatalytic test and kinetic study

The photocatalytic activity tests were carried out in batch system using a binary mixture of CV with MB dyes (CV:MB, with 44% CV and 56% MB, in mole fraction) as target molecules and the catalyst in suspension in a slurry reactor under visible irradiation (Bulb LED Lamp

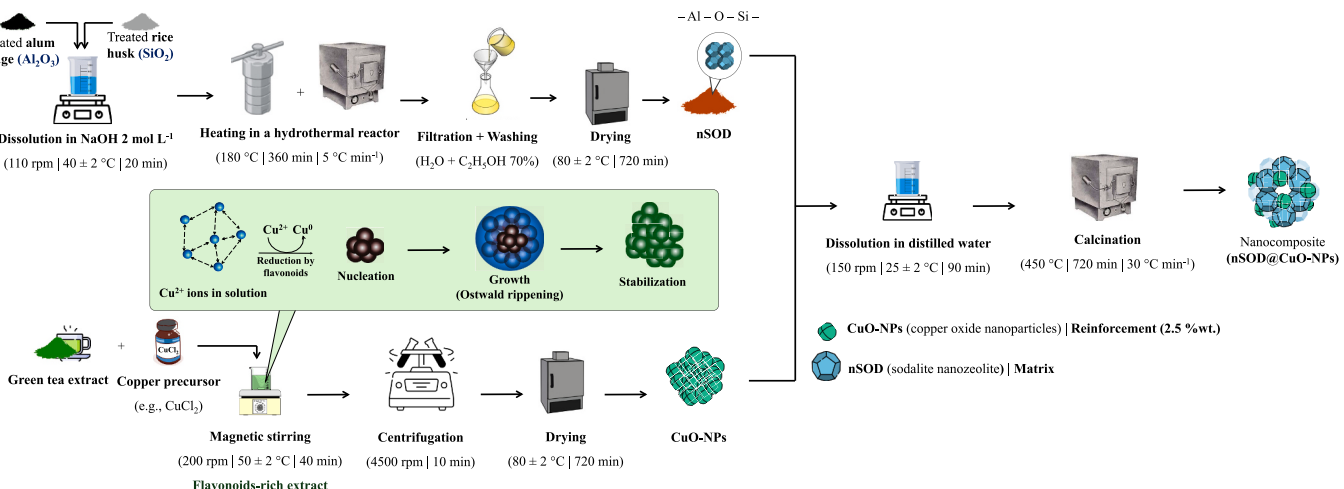


Fig. 1. Synthesis of the nSOD@CuO-NPs nanocatalyst. The nSOD@CuO-NPs nanocomposite was characterized by X-ray diffraction (XRD), Attenuated Total Reflectance-Fourier Transform Infrared Spectroscopy (ATR-FTIR), zero charge point (pH_{ZCP}) measurements, N_2 porosimetry, Dynamic Light Scattering (DLS) for the zeta potential (ZP) and particle size distribution (D_p) evaluation, Field Emission Gun – Scanning Electron Microscope (FESEM) with an Energy Dispersive X-ray Spectrometer (EDS), and Differential Reflectance Spectroscopy (DRS). Additionally, transmission electron microscopy (TEM) was employed using a Mira3 Tescan operating at 30 and 200 kV in STEM mode to characterize the morphology and distribution of average particle size of the synthesized nanomaterials. More information about characterization is provided in the Supplementary Information (SI).

Table 1

CCRD 2 experimental design for CV:MB photocatalytic degradation under visible radiation³

[CV:MB] (mg L ⁻¹)	[nSOD@CuO-NPs] (g L ⁻¹)	pH
(-1.68)	26	0.16
(-1)	70	0.5
0	135	1.0
(+1)	200	1.5
(+1.68)	244	1.84

with 50 W). The photocatalytic tests were carried out in two steps: (a) in dark condition: adsorption of the dyes mixture molecules onto the catalytic surface without irradiation (60 min), and (b) photocatalytic degradation of the CV:MB: under visible radiation: aliquots (~2 mL) were collected at time 0, 15, 30, 45, 60, 75, 90, 105, 120, 150 and 180 min, centrifuged (3500 rpm / 5 min) and diluted (1:10 v v⁻¹).

The absorbance was determined by UV-Vis spectrophotometer in three ways: (i) $\lambda = 590$ nm to investigate the CV dye as the target pollutant and MB dye as interferent; (ii) 663 nm to investigate MB dye as the target pollutant and CV dye as interferent; and (iii) at $\lambda = 630$ nm according to the molar composition of the binary mixture (44% CV and 56% MB dye). The dye degradation percentage was determined according to Eq. (1)

$$\%R = \left(\frac{A_0 - A_t}{A_0} \right) \times 100 \quad (1)$$

where: A_0 is the initial absorbance ($t = 0$); A_t is the absorbance at time t ; and %R is the degradation percentage of the organic dyes.

The apparent rate of the pseudo-first-order reaction (k) was determined using the Langmuir-Hinshelwood model, with linear regression of experimental data from Eq. (2) [25].

$$\ln \left(\frac{C_{i0}}{C_i} \right) = k^* t \quad (2)$$

where: C_{i0} is the initial dye concentration (mg L⁻¹); C_i is the dye concentration at time t (mg L⁻¹); k is the apparent rate of the pseudo first-order reaction (min⁻¹); and t is the reaction time (min).

2.5. Deep learning study

To predict dye absorbances at specific time intervals (0, 15, 30, 45, 60, 75, 90, 120, 150, 180, 210, and 240 min) for the photocatalytic degradation of crystal violet (CV) and methylene blue (MB) dye mixture and to investigate the influence of various variables on the predictions, a Multilayer Perceptron Artificial Neural Network (MLP-ANN) was employed. The dataset, generated using CCRD 2³ and nanocomposite characterization data, was organized in MS Excel and used as input for the neural network.

Twenty variables (pH, [nSOD@CuO-NPs], [CV:MB], reaction time (t_{rxn}), SBET, V_p , D_p , E_g , Al (%), Si (%), O (%), Cu (%), Fe (%), Cl (%), O (%), Na (%), C (%), ZP, and pH_{ZCP}) were used as input features. Absorbance (A) was set as the output variable. This selection allowed assessment of photocatalytic parameters and nanocatalyst properties on absorbance and consequently on degradation efficiency, $C C_0^{-1}$. All data were normalized to a 0–1 range before training. The dataset was split into training (70%) and testing (30%) subsets. The algorithm was implemented in Python 3.11.5, using Numpy, Pandas, TensorFlow, Keras, and Scikit-learn for computation, visualization, model building, and evaluation, respectively. More information about the dataset (file Dye mixture degradation nSOD@CuONPs.xlsx) is available on GitHub (<https://github.com/LeandroOviedo/Machine-and-Deep-Learning>).

Feature importance was analyzed by the Permutation Score method, quantifying each input variable's impact on model learning and prediction accuracy. Higher scores indicate greater influence on the photocatalytic degradation prediction [26]. Fig. 2 and Table 2 summarize all the steps involved in the deep learning study and the parameters tested in the algorithm.

The algorithm performances were evaluated in terms of the determination coefficient (R^2) and the Root Mean Squared Error (RMSE) was used as the loss function to validate the predictions, according to the Eqs. (7) and (8), respectively [28].

$$R^2 = 1 - \frac{\sum_{i=1}^N (y_{i,exp} - y_{i,pred})^2}{\sum_{i=1}^N (y_{i,exp} - \hat{y}_{i,pred})^2} \quad (7)$$

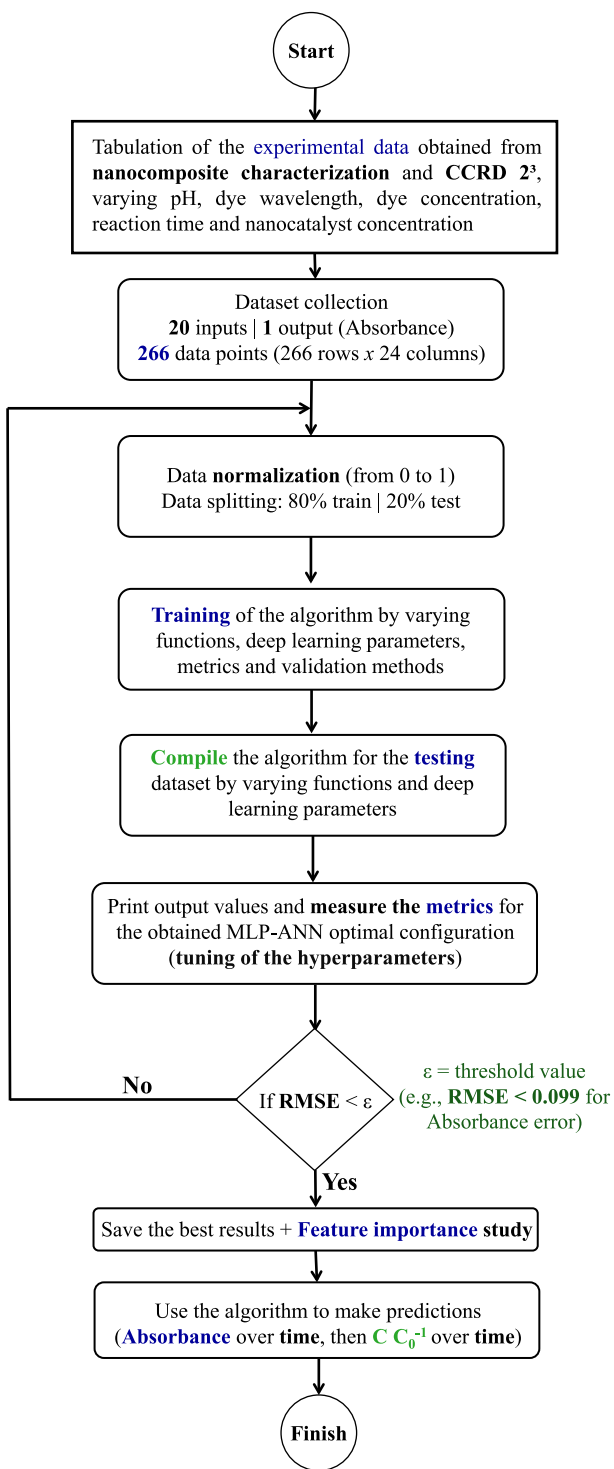


Fig. 2. Flowchart used to carry out the deep learning study.

$$RMSE = \sqrt{\frac{\sum_{i=1}^N (y_{i,exp} - \hat{y}_{i,pred})^2}{N}} \quad (8)$$

Where: $y_{i,exp}$ is the observed values (experimental data); $y_{i,pred}$ is the predicted data; $\hat{y}_{i,pred}$ is the predicted data associated with the response (absorbance); and N is the data size.

Table 2
Technical details of machine learning algorithms.

Algorithm parameters	Equations	Reference
Network structure:	Summation/transfer function (Eq. 3): $\varphi = \sum w_n \cdot x_n + b_k$ (3)	
Network 1: 20:10:10:1	Where: φ = transfer function; x_n = nth neural network node; w_i = weight associated with the nth neuron x_n ; b_k = bias (error associated with the prediction model); x = maximum value predicted by the ANN algorithm, using the ReLu function.	
Network 2: 20:10:12:1		
Network 3: 20:12:10:1		
Network 4: 20:12:12:1		
Network 5: 20:12:15:1		
Network 6: 20:15:12:1		
Network 7: 20:15:15:1		
Network 8: 20:15:18:1		
Network 9: 20:18:15:1	$f(\varphi) = (0, x_{max})$ (4)	[27]
Network 10: 20:18:18:1		
Network 11: 20:20:20:1	$f(\varphi) = \frac{1}{1 - e^{-\varphi}}$ (5)	
Network 12: 20:19:20:1		
Network 13: 20:20:19:1		
Network 14: 20:20:21:1	$f(\varphi) = \frac{2}{1 + e^{-2\varphi}} - 1$ (6)	
Network 15: 20:21:20:1		
Activation functions:		
reLu (Eq. 4), logistic (Eq. 5) and hyperbolic tangent (Eq. 6)	Where: φ = transfer function; x_n = nth neural network node; w_i = weight associated with the nth neuron x_n ; b_k = bias (error associated with the prediction model); x = maximum value predicted by the ANN algorithm, using the ReLu function	

Weight optimization function: lbfgs, Adam** | $cv = 5$ for all configurations tested

2.6. In vitro safety profile and statistical analysis

The in vitro safety profile was carried out with VERO cells (ATCC CCL-81), especially green monkey liver cells. Briefly, the in vitro assays were performed on CuO-NPs, nSOD, and nSOD@CuO-NPs samples to evaluate the cell viability (24 h of incubation) and proliferation (48 and 72 h of incubation) [29], ROS generation [30], NO generation [31] and determination of extracellular dsDNA release [32]. Statistical analysis and comparisons such as variance (one-way ANOVA) and the Dunnet test with $p < 0.033^*$, $p < 0.002^{**}$ and $p < 0.001^{***}$ were performed using the software's GraphPad Prism 8.0.1®. More information can be found in Supplementary Information (SI).

2.7. Ecotoxicity

The ecotoxicity of the samples (CuO-NPs, nSOD, and nSOD@CuO-NPs) was evaluated by the 72 h immersion of *Artemia salina* in a synthetic marine aqueous solution, according to the literature [33].

A. salina is often used in ecotoxicology as a model organism due to its rapid life cycle and high sensitivity to chemical compounds and contaminants [34]. Then, it is justified as the method selected to investigate the ecotoxicity of the nanomaterials prepared in this work. Thus, the acute toxicity of CuO-NPs, nSOD, and nSOD@CuO-NPs to *A. salina* was evaluated in four steps: (a) Preparation of artificial marine aqueous solution: 23 g of sodium chloride (NaCl, ACS reagent ≥99%, Dinâmica®), 11 g of magnesium chloride hexahydrate (MgCl₂·6H₂O, ACS reagent ≥99.0%, Sigma-Aldrich®), 0.4 g of sodium sulfate (Na₂SO₄, ACS reagent ≥99.0%, Synth®), 1.3 g calcium chloride dihydrate (CaCl₂·2H₂O, ACS reagent ≥99.0%, Sigma-Aldrich®), and 1 g potassium chloride (KCl, ACS reagent ≥99.0%, Sigma-Aldrich®) were mixed with 1 liter of distilled water and pH adjusted to 9 (with sodium carbonate – Na₂CO₃, ACS reagent ≥99.0%, Synth®); (b) Hatching of cysts: addition of 1.0 g of *A. salina* eggs containing 500 mL of marine aqueous solution followed by incubation in an oven with controlled temperature (28 ± 2 °C), and light (12h); (c) Preparation of concentrations: CuO-NPs, nSOD, and nSOD@CuO-NPs solutions (12.5, 25, 50, and 100 mg mL⁻¹), negative control (C-, marine aqueous solution and *A. salina*), and

positive control (C^+ , 0.01 mol L⁻¹ copper sulfate pentahydrate – CuSO₄•5H₂O, ACS reagent ≥99.0%, Synth®, and *A. salina*) and (d) Biotest: 10 mL of sample concentrations, 10 nauplii being placed in test tubes and kept in an oven (25 ± 2 °C / 48 h). Thus, after 72 h, the number of survived nauplii and hatched eggs was counted with a 20× magnifying glass and a 100× optical microscope. Statistical analysis was performed using one-way ANOVA followed by Tukey's post-hoc test to compare the effects of different concentrations of CuO-NPs, nSOD, and nSOD@CuO-NPs against the C+ group, with the C- group serving as the baseline. Significance levels were set at $p < 0.05^*$, $p < 0.01^{**}$, and $p < 0.001^{***}$. All analyses were conducted using GraphPad Prism software (version 9).

3. Results and discussion

3.1. Characterization of the nanocatalyst

Fig. 3 shows the XRD diffractograms, where nSOD@CuO-NPs showed crystalline phases of the catalytic support (analcime and sodalite) and crystalline phases of the photoactive phase (cuprite and tenorite). Analcime (Al₂H₄Na₂O₁₄Si₄, JCPDS n° 29-1132) was identified at $2\theta = 19^\circ, 28^\circ, 47^\circ, 48^\circ, 53^\circ, 55^\circ$, and 58° , whereas sodalite (C₂Al₆N₂Na₁₆O₂₄Si₆, JCPDS n° 43-1410) phase was observed at $2\theta = 17^\circ, 25^\circ, 31^\circ, 33^\circ$, and 35° . Regarding CuO-NPs ($d_c = 44.2$ nm), the peaks identified at $2\theta = 35^\circ, 38^\circ, 62^\circ, 67^\circ$ and 69° , and $2\theta = 32^\circ, 39^\circ, 49^\circ$ and 58° were associated to the tenorite (CuO, JCPDS n° 00-041-0254) and cuprite (Cu₂O, JCPDS n° 00-045-0937) crystalline phases, respectively [35,36].

Regarding crystallite diameter (d_c), nSOD exhibits the largest size ($d_c = 65$ nm), followed by the nSOD@CuO-NPs composite ($d_c = 50.4$ nm for the matrix and $d_c = 29.09$ nm for the CuO reinforcement), and CuO-NPs having the smallest crystallites ($d_c = 44.2$ nm). Generally, smaller crystallite sizes provide a higher specific surface area, increasing the number of active sites for catalytic reactions. In contrast, larger crystallites tend to offer greater structural stability but lower surface area. The composite's intermediate crystallite size reflects a balance between surface area and stability, optimizing photocatalytic efficiency. These effects are consistent with reports showing that crystallite size critically affects photocatalytic performance by modulating surface reactivity and charge dynamics [37].

Fig. 4 shows the ATR-FTIR spectra, in which the stretching and bending vibrations characteristic of zeolite in both nSOD and nSOD@CuO-NPs were identified.

According to **Fig. 4**, the following functional groups were identified:

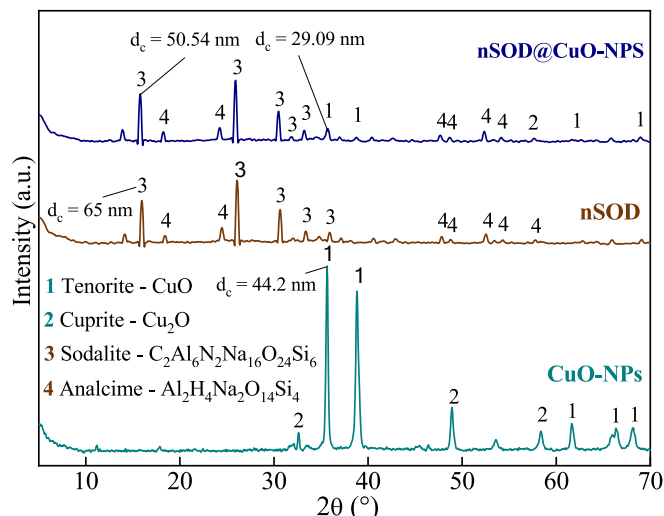


Fig. 3. XRD diffractograms for CuO-NPs, nSOD, and nSOD@CuO-NPs.

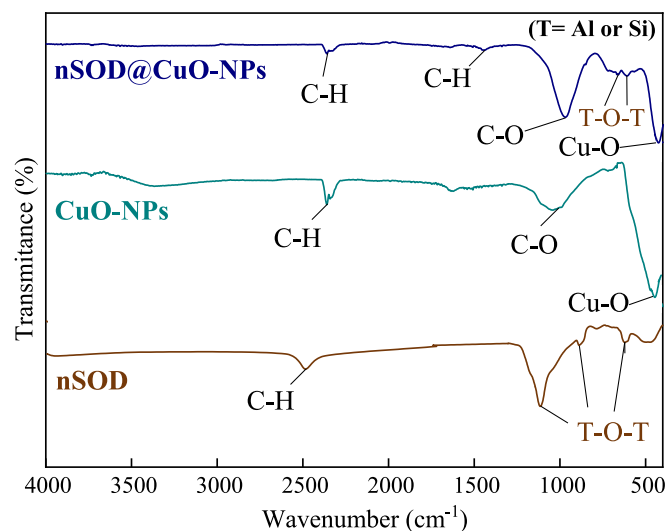


Fig. 4. ATR-FTIR spectra for CuO-NPs, nSOD, nSOD@CuO-NPs.

(a) at 2550 cm⁻¹ related to C–H vibrational stretching; (b) at 1465 cm⁻¹ associated with C–H vibrational bending from the alum sludge, (c) at 1163 cm⁻¹: C–O from aromatic ester corresponding to the compounds present in the green tea extract; (d) at 1250 cm⁻¹ associated with the internal stretching vibrations of T–O–T zeolitic framework, where T = Si or Al; (e) at 720–650 cm⁻¹, corresponding to the external bending vibration of the double rings of the tetrahedra framework (T–O–T, where T = Al or Si) [38], and (g) at 500 cm⁻¹ referring to the bending vibration of Cu–O [39].

Table 3 shows the textural (surface area – S_{BET}, pore volume – V_p, pore diameter – d_p) and surface (zeta potential – ZP) properties of the samples.

According to **Table 3**, the surface area (S_{BET}) of CuO-NPs increased from 1.9 to 14.8 m² g⁻¹ when they were incorporated into the nSOD to form the nSOD@CuO-NPs sample. This S_{BET} value remained close to nSOD (18.5 m² g⁻¹), indicating the successful incorporation of CuO-NPs while preserving the surface area of the catalytic support. This suggests an effective dispersion of copper oxide nanoparticles within the nSOD matrix, promoting a more homogeneous distribution of active sites for photocatalytic reactions.

The total pore volume (V_p) increased from 0.01 cm³ g⁻¹ in CuO-NPs to 0.04 cm³ g⁻¹ in nSOD@CuO-NPs, indicating an improved porosity due to the incorporation of CuO-NPs onto the nSOD support. This enhancement provides better mass transfer and accessibility of reactive sites during heterogeneous photocatalysis [40].

Nevertheless, the average pore diameter (d_p) of CuO-NPs (43.1 nm) decreased significantly in nSOD@CuO-NPs (16.7 nm), suggesting a redistribution of the porous network upon CuO-NPs incorporation. Moreover, a reduction in pore size can improve the adsorption capacity of the catalyst, as smaller pores can effectively trap reactant molecules, resulting in higher concentrations of these molecules at the active sites during the photocatalytic process [41].

Overall, the structural changes associated with smaller pores may also influence the electronic properties of the catalyst. A well-structured

Table 3
Textural properties (S_{BET}, V_p and d_p) and zeta potential (ZP) of the samples.

Samples	S _{BET} (m ² g ⁻¹)	V _p (cm ³ g ⁻¹)	d _p (nm)	ZP (mV)
CuO-NPs	1.9 ± 0.01	0.01 ± 0.002	43.1 ± 7.8	-2.6 ± 1.2
nSOD	18.5 ± 0.8	0.034 ± 0.001	12.7 ± 0.84	-34.0 ± 1.1
nSOD@CuO-NPs	14.8 ± 0.7	0.04 ± 0.001	16.7 ± 0.7	-18.5 ± 1.0

porous network can help minimize electron-hole pair recombination, thereby increasing the efficiency of charge carriers during photocatalytic reactions [42].

The zeta potential (ZP) values provide insights into the stability and dispersibility of these nanomaterials in suspension. The negative and high zeta potential values (e.g., near -30 mV) indicate good stability, which is important for maintaining an effective photocatalytic system by preventing agglomeration during reactions [43]. According to Table 2, the CuO-NPs showed a lower ZP and, hence, lower physicochemical stability. In contrast, a higher value of ZP (-34 mV) was reported for nSOD, suggesting high physicochemical stability of the catalytic support. Thus, the incorporation of the CuO-NPs in the nSOD resulted in the stabilization of the active phase ($ZP = -18.5$ mV), which confirms good physicochemical stability of the synthesized nanocatalyst and can be helpful in preventing nanocatalyst particle agglomeration in the aqueous medium.

The minimal change in zeta potential (ZP) observed after incorporating CuO-NPs into the nSOD support suggests that the surface properties of the support remain largely unchanged. This implies that the interaction between CuO-NPs and the nSOD support is probably physical rather than chemical, since significant chemical bonding would typically cause more pronounced alterations in surface charge. This fact is supported by the literature, where other supported nanocatalysts synthesized via impregnation methods (e.g., typically involving calcination at $400\text{--}600$ °C) undergo crystallization and removal of organic residues during calcination, but do not necessarily form strong chemical bonds between the components, resulting in composites characterized predominantly by physical interactions [44]. Therefore, it can be inferred that the nSOD support is not chemically bound to the CuO-NPs, preserving its original surface characteristics and contributing to the overall stability of the nanocatalyst. The zero charge point (pH_{ZCP}) of the nanocatalyst and its counterparts is provided in Fig. 5.

According to Fig. 5, CuO-NPs showed $pH_{ZCP} = 7.46$, whereas $pH_{ZCP} = 8.36$ was reported for nSOD. Moreover, nSOD@CuO-NPs showed a $pH_{ZCP} = 7.65$, an intermediate value. The pH_{ZCP} provides information about the pH range at which the nanocatalyst surface will be protonated (positively charged, pH_{ZCP}) or deprotonated (negatively charged, $pH > pH_{ZCP}$) [45]. Thereafter, it can be used to get insight into the strength or type of electrostatic interactions (e.g., attraction or repulsion) between the target pollutant molecules and the nanocatalyst.

According to the results, at $pH > 7.65$, the surface of the nSOD@CuO-NPs will be deprotonated, resulting in higher electrostatic interactions (attraction) between cationic dye molecules and the

nanocatalyst, and hence, higher MB and CV degradation. In contrast, at $pH < 7.65$ and acidic pHs, the CV and MB degradation will not be favored due to higher electrostatic repulsion between the dye molecules and the nSOD@CuO-NPs [46]. Figs. 6(a)–6(f) show the FEG-SEM micrographs with EDS results to inform the samples' morphology and chemical composition, respectively.

According to Figs. 6(a), CuO-NPs showed an irregular morphology divided into some clusters, whereas the nSOD (Fig. 6c) was identified as regular spheres, which is typical of sodalite [47,48]. Thus, the morphology of nSOD@CuO-NPs (Fig. 6e) identified sodalite spheres with CuO-NPs clusters dispersed onto their surfaces, confirming that the impregnation of copper oxide nanoparticles onto the nanozeolite was successfully obtained.

Moreover, according to Fig. 6(b), CuO-NPs showed the elemental composition: Cu (69.9 wt%), O (23.3 wt%), C (4.2 wt%), Cl (2.3 wt%), and K (0.3 wt%). Carbon, chloride, and potassium were probably due to the green tea extract and non-reacted $CuCl_2 \cdot 2H_2O$ in the green synthesis. The spectrum of the nSOD (Fig. 6d) reported C (22.8 wt%), O (44.7 wt%), Si (10.5 wt%), Na (8.8 wt%), Al (7.7 wt%), Fe (4.1 wt%), and 0.8 wt% of other minor components as the elemental composition. Carbon and iron identified in the nSOD composition were probably from residual sources, especially the alum sludge, in which ferric chloride and ferric hydroxide are commonly present [47]. Additionally, Fig. 6(f) reports the following elemental composition for nSOD@CuO-NPs: C (23.7 wt%), O (41.1 wt%), Si (10.6 wt%), Na (8.8 wt%), Al (8.4 wt%), Fe (4.0 wt%), Cu (2.1 wt%) and 1.1 wt% corresponding to minor components (e.g., K, Mg, Ca, and Cl), respectively. The copper content confirmed the successful obtention of the desired nanocomposite, a hybrid nanocatalyst. It is worth mentioning that the measured Si/Al ratio for the nSOD and nSOD@CuO-NPs was 1.26 and 1.36, which is typically found for sodalite and confirms that the synthesized nanozeolite is a low-silica zeolite [48–50]. Figs. 7(a), 7(c), and 7(e) present the TEM micrographs, revealing the morphology and aggregation characteristics of each material, whereas Figs. 7(b), 7(d), and 7(f) quantify the distribution of average particle size.

The CuO-NPs (Fig. 7a) appear as roughly spherical particles with some degree of aggregation. The nSOD (Fig. 7c) displays more irregular and clustered structures, suggesting higher aggregation. In contrast, the nSOD@CuO-NPs composite (Fig. 7e) exhibits smaller, more uniformly dispersed particles, indicating improved dispersion and less aggregation compared to the individual components.

The particle size distribution histograms (Figs. 7b, 7d, and 7f) reveal that the mean particle diameter is $D_p = 24.90 \pm 6.70$ nm for CuO-NPs (Fig. 6b), $D_p = 28.01 \pm 20.4$ nm for nSOD (Fig. 7d), and $D_p = 20.2 \pm 14.21$ nm for nSOD@CuO-NPs (Fig. 7f). Notably, the composite material shows a clear reduction in mean particle diameter and a narrower size distribution. According to recent literature, such a decrease in particle size upon combining nanomaterials can enhance catalytic activity due to the increased surface area and improved dispersion, which facilitates better interaction with reactants [51]. Fig. 8 presents the D_p evaluated by DLS characterization.

The DLS results in Fig. 8 are consistent with the literature for nanomaterials, where CuO-NPs show the smallest average diameter ($D_p = 88.28$ nm), indicating good dispersion, while nSOD exhibits a much larger size ($D_p = 790.30$ nm) due to aggregation, as commonly reported for porous supports [52]. The intermediate size of nSOD@CuO-NPs ($D_p = 200.60$ nm) suggests improved dispersion upon nanoparticle loading, in line with recent studies on nanocomposites [53].

Fig. 9 informs the band gap energy (E_g) for the nanocatalyst and its counterparts.

According to Fig. 9a and c, the E_g of CuO-NPs and nSOD@CuO-NPs were 1.80 eV and 1.38 eV, respectively. In contrast, as observed in Fig. 9b, no one value for E_g was reported for nSOD, since no linear region of the DRS spectrum was observed. The E_g of CuO-NPs was consistent with literature values for green copper oxide [54,55]. Moreover, the impregnation of CuO-NPs into nSOD reduced the E_g value. This

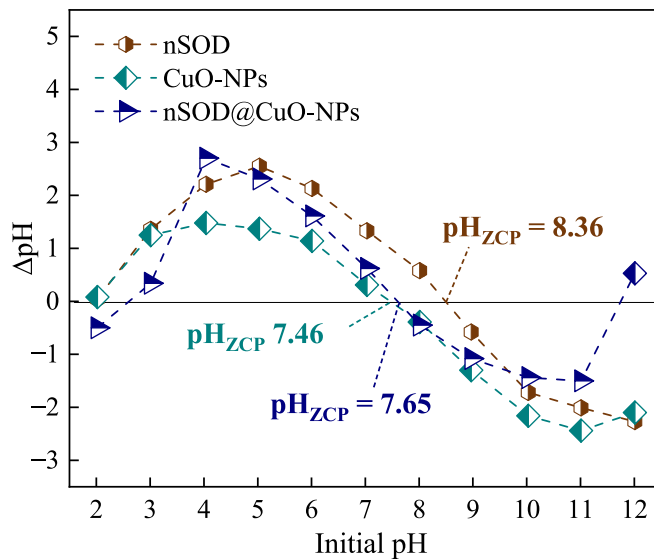


Fig. 5. Zero charge point (pH_{ZCP}) of CuO-NPs, nSOD, and nSOD@CuO-NPs.

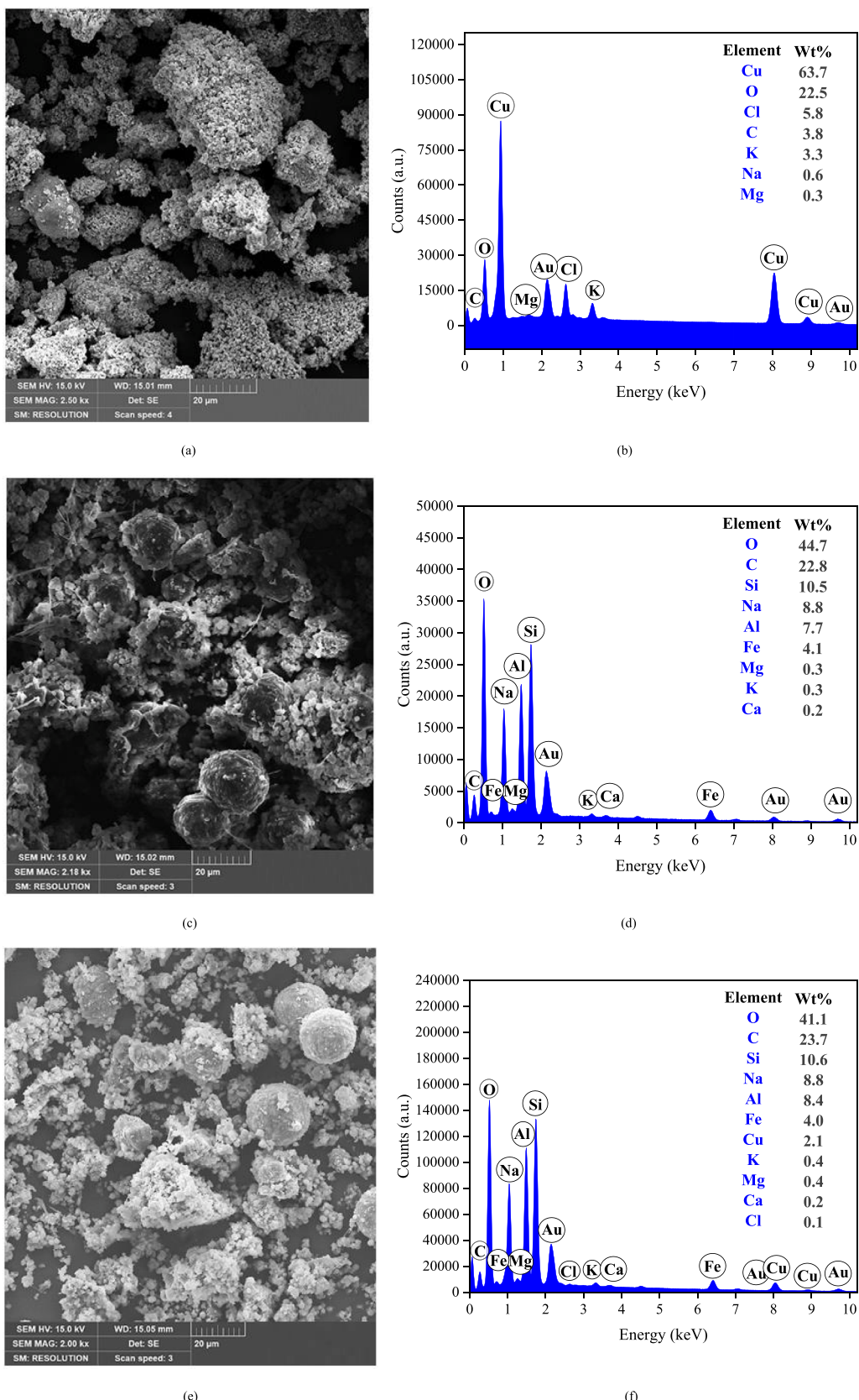


Fig. 6. FEG-SEM micrographs of (a) CuO-NPs with 2.5 kx magnification, (c) nSOD with 2.18 kx magnification, and (e) nSOD@CuO-NPs with 2 kx magnification. EDS results of the (b) CuO-NPs, (d) nSOD, and (f) nSOD@CuO-NPs.

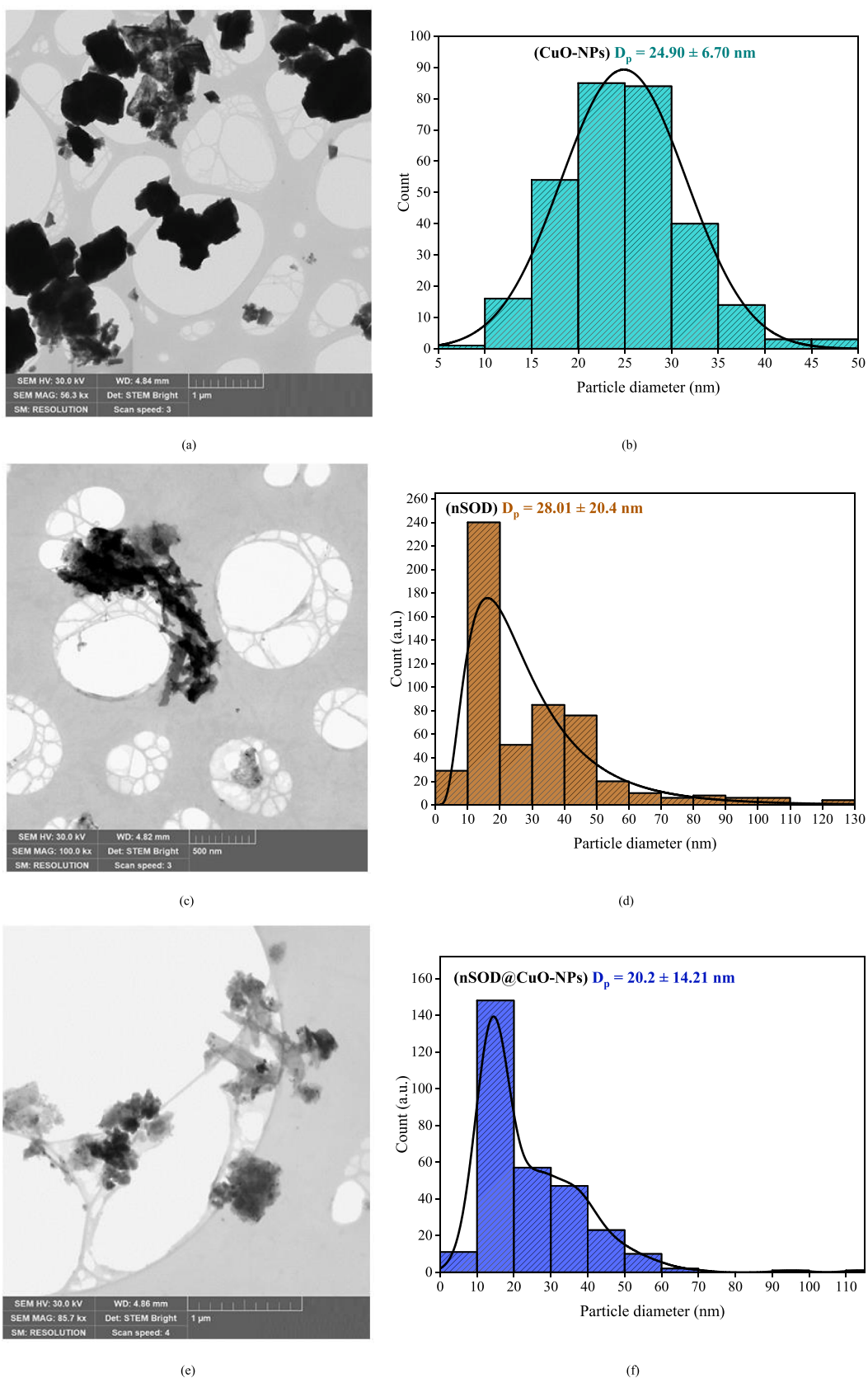


Fig. 7. TEM micrographs of (a) CuO-NPs with 56.3 kx magnification, (c) nSOD with 100 kx magnification, and (e) nSOD@CuO-NPs with 85.7 kx magnification. Distribution of average particle size of the (b) CuO-NPs, (d) nSOD, and (f) nSOD@CuO-NPs.

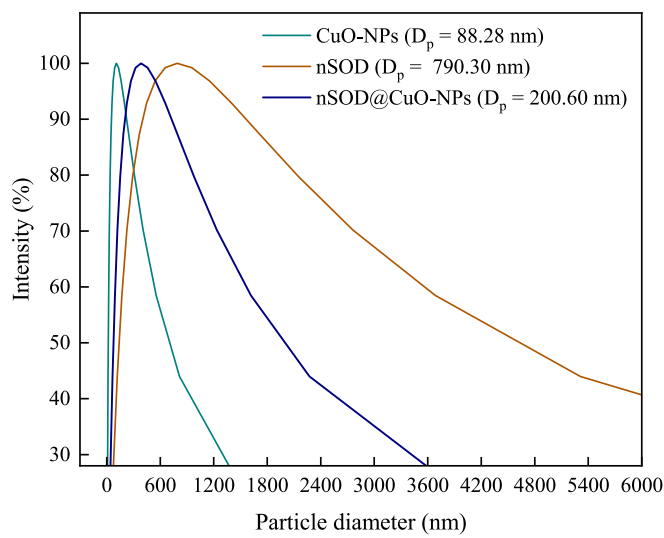


Fig. 8. Particle size distribution (D_p) of CuO-NPs, nSOD, and nSOD@CuO-NPs evaluated by DLS.

reduction in the E_g value implies enhanced photocatalytic activity of the nanocatalyst by enabling it to absorb a broader range of UV-Vis wavelengths [56].

Additionally, reduced E_g can facilitate better charge separation, reducing the recombination rate of electron-hole pairs and further boosting photocatalytic efficiency [57]. Thereafter, these findings confirm that the synthesized hybrid nanocatalyst showed enhanced stability and photocatalytic activity than CuO-NPs, as well as characterize the nSOD as a good catalytic support.

3.2. Photocatalytic activity of nSOD@CuO-NPs and kinetic study

Table 4 shows the dataset obtained from the CCRD 2³ developed to evaluate the ideal condition of the heterogeneous photocatalysis process.

According to Table 4, the ideal condition of the heterogeneous photocatalysis process was identified in Run 17 (at pH 10, [CV:MB] = 70 mg L⁻¹, [nSOD@CuO-NPs] = 1.5 g L⁻¹), yielding 84.5% degradation for CV:MB after 180 min. In this run, 79.4% and 82.9% were reported for CV and MB dye after 180 min under visible radiation.

Fig. 10 informs the surface response generated by CCRD 2³ to illustrate the effect of dye mixture and nanocatalyst concentrations on the %R.

According to Fig. 10, there was an optimum value for %R when the concentration of [CV:MB] approached 150 mg L⁻¹ and the concentration of [nSOD@CuO-NPs] approached 1.0 g L⁻¹. Moreover, the surface response revealed that at [CV:MB] = 90–180 mg L⁻¹ and [nSOD@CuO-NPs] = 0.8–1.25 g L⁻¹ ranges, the degradation percentage (%R) is higher. Thus, optimizing the balance between dye concentration and nanocatalyst concentration can enhance the degradation efficiency.

Studies in the literature indicated that increased dye concentrations can enhance the interaction with the active sites on the catalyst surface, promoting degradation up to a certain threshold [58]. The concentration of 1.0 g L⁻¹ for nSOD@CuO-NPs probably provides the optimal number of active sites to accommodate the dye molecules without causing significant agglomeration, thereby maximizing the number of available sites for degradation. Similarly, Fig. 11 shows the surface response generated by CCRD 2³ to illustrate the effect of dye mixture concentration and pH on the %R.

According to Fig. 11, high %R values are achieved at pH 5–9 and [CV:MB] = 70–170 mg L⁻¹. A slightly acidic to basic pH (5–9) enhances both dye adsorption and the generation of reactive oxygen species (ROS) from the CuO catalyst [59]. Outside this range, either electrostatic repulsion

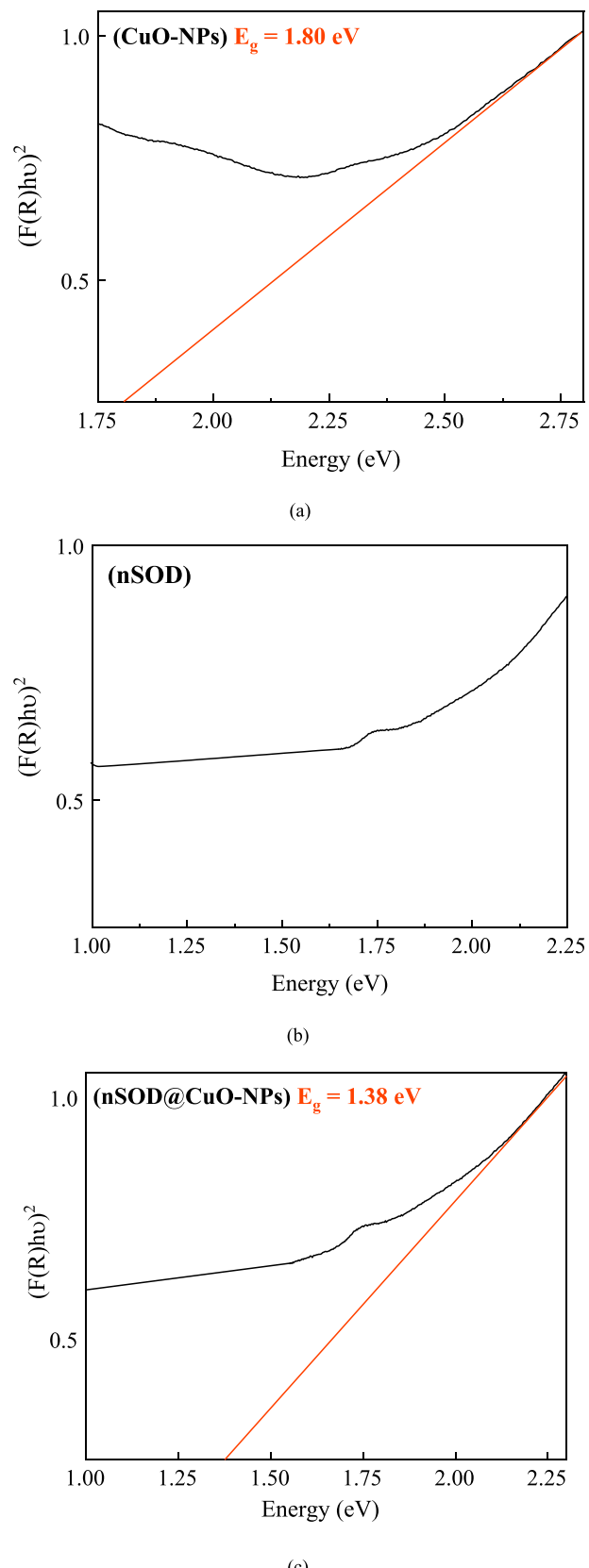


Fig. 9. Band gap energy (E_g) of CuO-NPs, nSOD, and nSOD@CuO-NPs.

Table 4

CCRD 2³ results for CV:MB binary mixture photocatalytic degradation under visible radiation.

Run	[CV:MB] (mg L ⁻¹)	[nSOD@CuO-NPs] (g L ⁻¹)	pH	%R (CV) nm	%R (MB) nm	%R λ = 630 nm
1	200.0	0.5	10	47.5	62.2	60.2
2	135.0	1.0	2	66.0	53.5	59.0
3	135.0	1.0	7	79.7	82.2	81.8
4	244.3	1.0	7	52.5	68.2	65.0
5	135.0	1.0	12	39.9	48.3	46.5
6	200.0	1.5	10	55.0	63.0	60.7
7	70.0	1.5	4	59.4	42.4	52.0
8	135.0	0.2	7	52.5	72.2	68.8
9	135.0	1.0	7	65.0	78.0	77.9
10	135.0	1.0	7	66.0	77.6	78.0
11	135.0	1.8	7	58.0	42.0	52.0
12	70.0	0.5	4	68.0	72.5	72.7
13	200.0	0.5	4	49.5	58.1	56.1
14	200.0	1.5	4	57.8	65.3	63.0
15	70.0	0.5	10	35.6	26.7	31.4
16	25.7	1.0	7	45.3	36.8	41.6
17	70.0	1.5	10	79.4	82.9	84.5

Reaction time set for all experiments: 180 min.

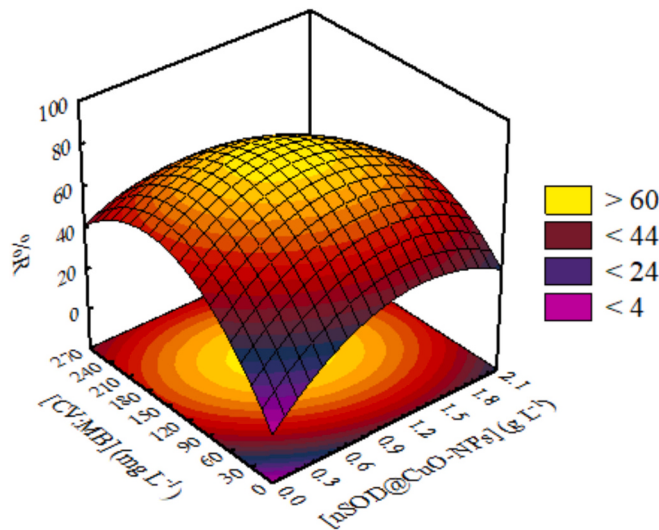


Fig. 10. 3D response surface of the dye mixture ([CV:MB]) and nanocatalyst ([nSOD@CuO-NPs]) concentrations for the photocatalytic degradation process.

becomes dominant (low pH) or ROS generation is inhibited due to hydroxyl radicals ($\text{HO}\cdot$) recombination (high pH) [60]. Similarly, the optimal [CV:MB] range reflects a balance; too low a concentration limits the available dye molecules for degradation, while too high a concentration leads to light screening and reduced catalyst activity, in line with findings on dye concentration effects on photocatalytic efficiency [61]. Figs. 12(a) and 12(b) illustrate the degradation kinetics of the CV:MB dye mixture under different photocatalytic systems: CuO-NPs, nSOD, nSOD@CuO-NPs, and photolysis as a control, with all systems operating in the ideal conditions evaluated in the CCRD 2³.

The results in Fig. 12 demonstrate that the nSOD@CuO-NPs composite exhibits the highest degradation efficiency for both dyes at the respective wavelengths, as indicated by the steeper decline in normalized concentration over time. Thus, 79.4% ($\lambda = 590 \text{ nm} / k = 0.098 \text{ min}^{-1}$) and 82.9% ($\lambda = 663 \text{ nm} / k = 0.108 \text{ min}^{-1}$) for CV:MB dye degradation after 180 min were observed. In contrast, photolysis shows the slowest degradation (14.5% at $\lambda = 590 \text{ nm}$, with $k = 0.0009 \text{ min}^{-1}$ / 26.2% at $\lambda = 663 \text{ nm}$, with $k = 0.0019 \text{ min}^{-1}$), highlighting the necessity of a photocatalyst for effective dye removal. The superior performance

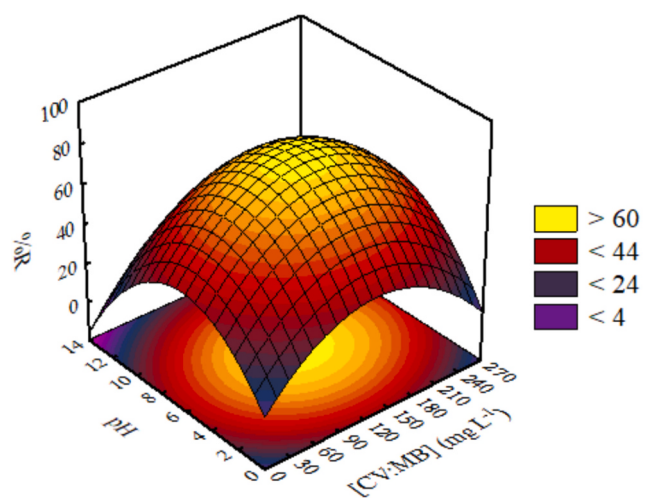


Fig. 11. 3D response surface of the dye mixture concentration ([CV:MB]) and pH for the photocatalytic degradation process.

of nSOD@CuO-NPs can be attributed to the synergistic effect between the nSOD support and the CuO nanoparticles. This combination probably enhances charge separation and provides more active sites for photocatalytic reaction, resulting in faster dye degradation [62].

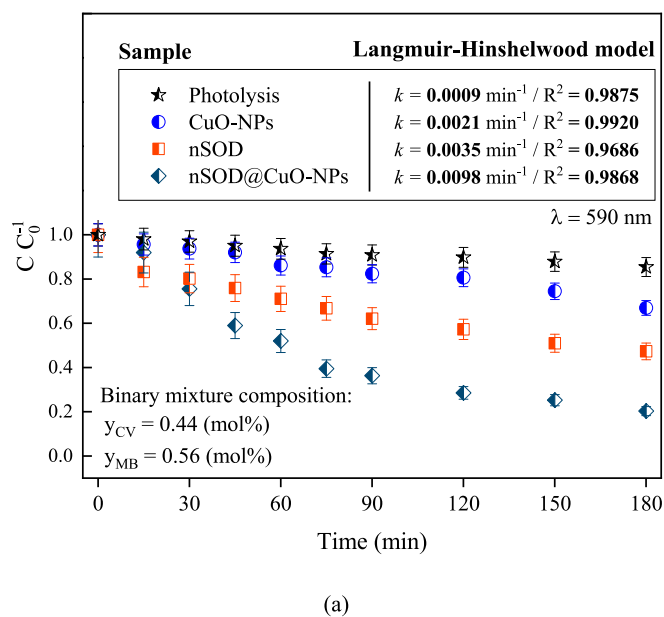
In parallel, the intermediate performance of CuO-NPs (33.0% at $\lambda = 590 \text{ nm} / k = 0.021 \text{ min}^{-1}$ / 47.7% at $\lambda = 663 \text{ nm}$, with $k = 0.0039 \text{ min}^{-1}$) and nSOD (41.6% at $\lambda = 590 \text{ nm} / k = 0.035 \text{ min}^{-1}$ / 51.2% at $\lambda = 663 \text{ nm}$, with $k = 0.0043 \text{ min}^{-1}$) suggests that, while each material possesses catalytic activity, their combination in the composite structure significantly improves overall efficiency. This improvement is probably due to better dispersion of the active phase and reduced electron-hole recombination, leading to enhanced photocatalytic activity [63].

To investigate the influence of each parameter in heterogeneous photocatalysis, a Pareto chart was generated from the CCRD 2³, whose results are shown in Fig. 13.

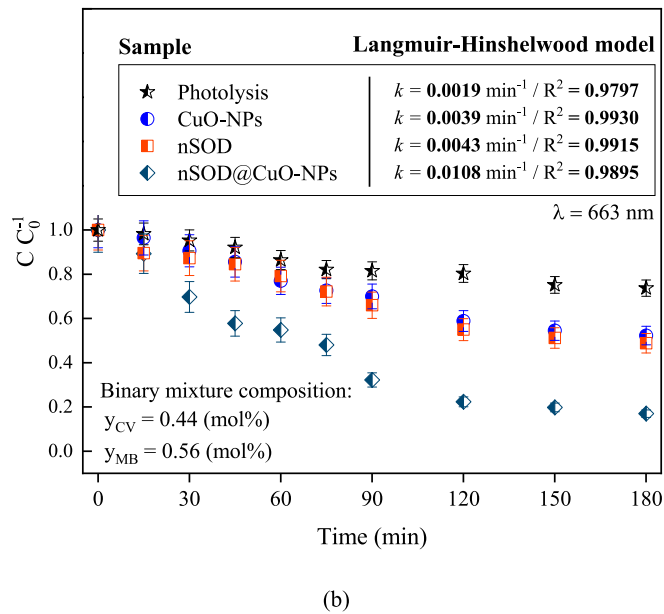
According to Fig. 13, the most influential factors (exceeding the $p = 0.05$ threshold), in the dye binary mixture photocatalytic degradation, in descending order, were: quadratic effect of the pH (pH^2) > quadratic effect of the dye mixture concentration ($[\text{CV:MB}]^2$) > the interaction between the nanocatalyst and the pH ($[\text{nSOD@CuO-NPs}] * \text{pH}$) > quadratic effect of the nanocatalyst concentration ($[\text{nSOD@CuO-NPs}]^2$) > the dye mixture concentration ($[\text{CV:MB}]$). The negative signs associated with the pH^2 and $[\text{CV:MB}]^2$ indicate an inverse relationship between these quadratic terms and the response variable, implying that there is an optimal range for both pH and [CV:MB] variables. Thus, exceeding or falling below this optimal range negatively, the degradation efficiency can be reduced.

The interaction between nSOD@CuO-NPs and pH suggests that the effect of catalyst concentration on degradation is pH-dependent. Factors falling below the $p = 0.05$ threshold (such as the linear effect of pH, $[\text{CV:MB}] * \text{pH}$, and $[\text{nSOD@CuO-NPs}]$) have statistically insignificant effects on the degradation within the experimental design parameters. Therefore, optimizing pH and the [CV:MB], while considering the interaction between catalyst concentration and pH, should be prioritized for maximizing degradation efficiency.

To investigate these patterns, an ANOVA was performed to verify the prediction ability of the CCRD 2³. Thus, it was verified that the model shows moderate predictive capability since F_{CAL} (1.0) was smaller than F_{TAB} (3.68), with the model explaining 57.38% of the variability in experimental data. This is probably due to the limited number of variables considered in the analysis, which is insufficient to identify patterns in the data and, consequently, does not adequately reproduce the experimental observations. Additionally, experimental noise, non-linear interactions, and other factors beyond pH, nanocatalyst, and dye



(a)



(b)

Fig. 12. Kinetic curve for CV:MB dye mixture at (a) $\lambda = 590$ nm (CV – target pollutant / MB – interferent), and (b) $\lambda = 663$ nm (MB – target pollutant / CV – interferent). (Operational parameters: [nanocatalyst] = 1.5 g L^{-1} , [CV:MB] = 70 mg L^{-1} , pH 10).

concentrations are probably influencing the predictive capability of the model. To investigate further, a deep learning study was carried out to find important observations/patterns within the process and to get predictions of absorbance over time (and $C C_0^{-1}$) for enhancing the reproducibility of the experimental data.

3.3. Deep learning

Deep learning algorithms were used to identify patterns within the experimental observations obtained from the CCRD 2³ and nano-composite characterizations dataset. Deep learning can capture hidden patterns that govern data behavior and comprehend and reproduce complex situations, such as the photocatalytic degradation of organic pollutants in bicomponent systems (e.g., binary dye mixture investigated in this work). Thereafter, it was possible to address the variables

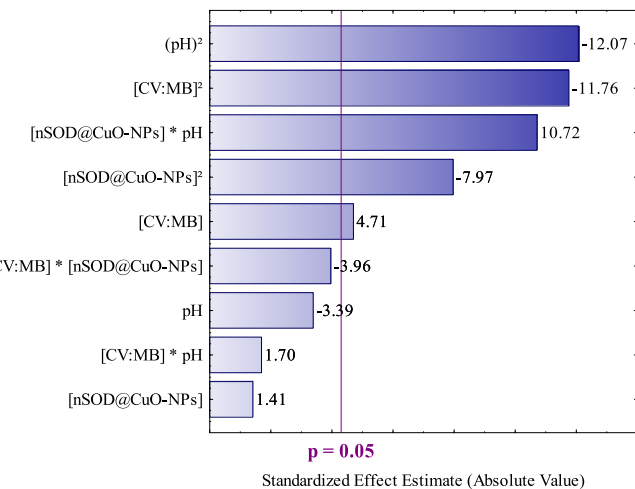


Fig. 13. Pareto chart developed from CCRD 2³.

that affect the process and to make predictions for experimental conditions within and beyond the experimental set provided to the machine.

Initially, a feature importance analysis was carried out to identify the variables that affect the degradation of CV and MB dyes in a bicomponent system, using nSOD@CuO-NPs nanocatalyst, according to the MLP-ANN algorithm. Fig. 14 shows the results of the Permutation Score for each variable. The greater the Permutation Score for a variable, the higher the influence of this variable on the prediction and, hence, on the process.

According to Fig. 14, the feature importance analysis reported 2.49 as the threshold, which serves as a benchmark to distinguish significant, moderate, and low-impact variables. Variables exceeding this threshold have a substantial influence on the degradation process, while those near it exhibit moderate or minimal effects.

Thus, according to Fig. 14, all the parameters (except sodium content – Na (%), and Si/Al ratio) showed influence on the algorithm predictions (of absorbance value and, hence, $C C_0^{-1}$). Thus, the following order of the importance of the parameters was dye wavelength (λ) > pH > dye mixture concentration ([CV:MB]) > reaction time (t_{rxn}) > surface area (S_{BET}) > catalyst concentration ([nSOD@CuO-NPs]) > Band gap energy (E_g) > zeta potential (ZP) > Pore diameter (D_p) > catalyst impurities – C (%) and Fe (%) > Pore volume (V_p) > Chloride content, Cl (%) > Oxygen content, O (%) > Zero charge point (pH_{ZCP}) > Si (%) > Al (%) > Cu (%), respectively.

In summary, the properties of the organic pollutants (e.g., dye wavelength), photocatalytic process parameters (pH, t_{rxn} , [CV:MB], [nSOD@CuO-NPs]), textural/surface/optical properties (S_{BET} , V_p , d_p , ZP, pH_{ZCP} , E_g) and some impurities of the catalyst (C, Fe, Cl and O content) show significance to the algorithm in the prediction of absorbance of dye mixture over time. Thus, the most impactful variables include dye wavelength, pH, dye mixture concentration, reaction time, surface area, catalyst concentration, and band gap energy, all of which exhibit permutation scores above 3.5. In this view, ZP, V_p , d_p , and impurities Fe (%) and C (%) showed a moderate influence on the algorithm predictions, with the remaining variables showing a low effect.

The dye wavelength reflects the maximum absorbances for CV ($\lambda = 590$ nm) and MB ($\lambda = 663$ nm), directly affecting the light absorption and subsequent photodegradation. Reaction time (t_{rxn}) plays a critical role in determining the dye absorbance, as longer exposure allows for higher interaction between the catalyst and reactive species. Absorbance commonly reduces with time during the reaction, indicating degradation of the organic pollutants as time elapses until complete mineralization [64].

Dye mixture concentration affects the prediction in the following manner: low concentrations limit available dye molecules for reaction,

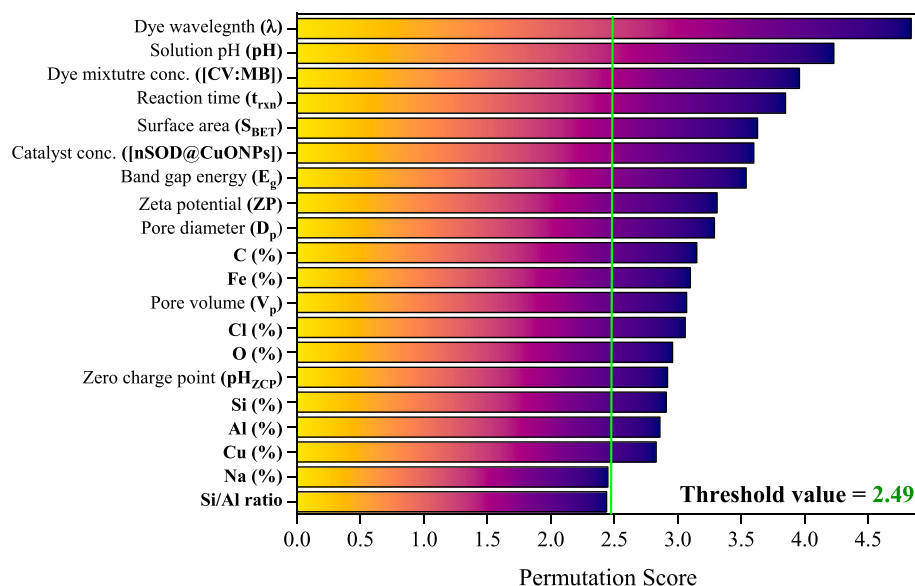


Fig. 14. The influence of each parameter on the photocatalytic degradation of a dye binary mixture, based on the feature importance analysis and MLP-ANN algorithm.

while high concentrations cause light screening, reducing catalyst activity [65]. Thus, concentrations too low and too high concentrations can compromise the prediction.

Regarding catalyst concentration, higher catalyst concentrations increase active sites but can lead to agglomeration, reducing efficiency. Thus, an optimal balance ensures maximum interaction between dyes and reactive species. Therefore, the concentration range used in this work seems to be suitable for making deep learning predictions.

pH significantly affects the surface charge of the catalyst, influencing adsorption and radical generation and, hence, the absorbance (and $C_{0^{-1}}$ value). The band gap energy determines light absorption and electron-hole pair generation. A low E_g enhances visible-light-driven photocatalysis, improving degradation rates for MB and CV, thus interfering with the absorbance reading.

Carbon and iron impurities can have a negative impact on the absorbance reading since they influence electron transfer dynamics, enhancing or inhibiting catalytic activity depending on their concentration. Thus, they can affect absorbance reading and predictions. Chloride ions can act as scavengers for free radicals ($\bullet\text{OH}$ and $\bullet\text{O}_2^-$), reducing efficiency, while oxygen promotes oxidation reactions [66]. Thus, although Cl (%) showed moderate significance to the algorithm, higher chloride content can influence the absorbance value prediction by affecting the photocatalytic efficiency and radical generation during the degradation process. Additionally, chloride ions can be released in the aqueous medium and form subproducts that absorb light on wavelengths very close to the dye characteristic wavelengths [67]. Moreover, different Fe (%) contents are present in nSOD@CuO-NPs, related to nanozeolite from different batches. Iron can aid the photodegradation of

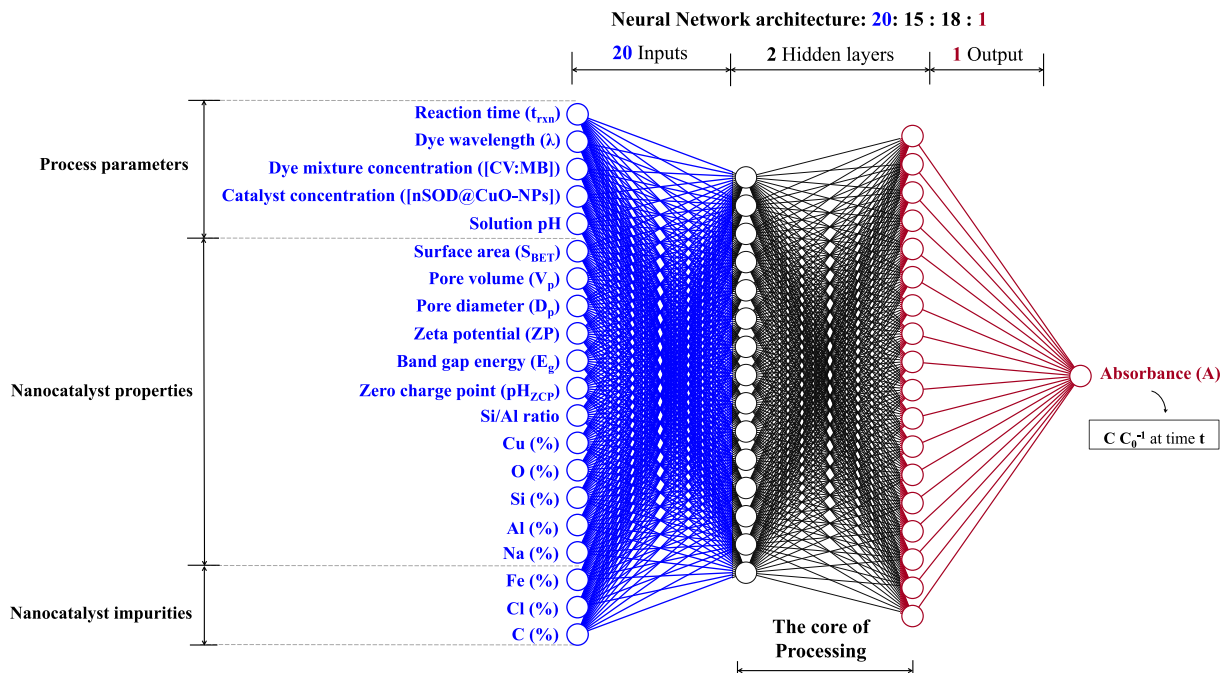


Fig. 15. Optimal neural network configuration for absorbance prediction.

the dye mixture since it can be changed by Al atoms in the nanozeolitic framework, increasing the acidity of the nanocomposite matrix [68].

Despite having a minimal direct impact on photocatalytic activity compared to other parameters, silicon and aluminum contents contribute to properties (e.g., acidity) and structure (porous network and topology) of the nanozeolite and then to the nanocomposite stability and properties [69].

Therefore, balancing the values of the input parameters in a consistent manner with experimental observations can ensure good and reliable predictions of the heterogeneous photocatalysis in bicomponent systems for different scenarios. Based on it, an optimized architecture of the neural network was developed. Thus, Fig. 15 illustrates this optimized configuration, while Fig. 16 reports the best result found in the deep learning study in terms of the performance and learning profile of the MLP-ANN algorithm.

According to Figs. 15 and 16, the MLP-ANN algorithm showed satisfactory performance in the absorbance prediction (and hence, degradation reaction progress), with the following neural network architecture: 20 input variables: 15 neurons in the first hidden layer; 18 neurons in the second hidden layer; 1 output variable (response). The good performance of the algorithm learning is attributed to the similarity of the determination coefficient for training ($R^2 = 0.9222$) and testing ($R^2 = 0.9149$) data as well as the proximity and low values of RMSE_{training} (0.071) and RMSE_{testing} (0.077) which indicates a low probability of overfitting in the deep learning. Moreover, as shown in Fig. 16, the RMSE reached a plateau after 40 epochs. This result suggests that the machine is learning well from data and is doing an excellent job in the generalization task (i.e., predicting new data). Furthermore, predictions of new data were carried out to get absorbance beyond the time interval used in the experimental runs, whose values are reported in Table 5.

According to Table 5, the algorithm showed a low relative error in the prediction in 180, 210, and 240 min. However, at higher times ($t_{rxn} > 240$ min), the relative error increases, and then the predictions were evaluated from 0 to 240 min. In addition, it was observed that the predicted absorbance values (and $C C_0^{-1}$) reduce as time increases. This pattern shows good coherence with experimental data reported in the literature dealing with photocatalytic degradation of synthetic dyes [70].

Figs. 17(a) and 17(b) show the prediction of the photocatalytic degradation for CV and MB dyes under visible radiation after 240 min.

Fig. 17(a), ~79% CV dye degradation is achieved up to 180 min and reaches a plateau after 240 min, suggesting that the maximum

Table 5
Predictions carried out with MLP-ANN algorithm.

Time (min)	Y_{pred}	Y_{obs}	Error
180	0.168	0.139	3%
210	0.146	0.147	0.6
240	0.127	0.115	1%
270	0.108	0.104	4%
300	0.089	0.035	5%

Predictions performed for CV:MB dye mixture at $\lambda = 630$ nm. Operational parameters: Activation function = ReLU | weight updating function = AdamW | initial learning rate of 0.1% | neural network: 20:15:18:1 (20 inputs, 2 hidden layers with 15 and 18 neurons each, and 1 response). | $R^2 = 0.89$ and RMSE = 0.082.

photocatalytic activity of the nSOD@CuO-NPs nanocatalyst under visible radiation is achieved. Similarly, the degradation curve shown in Fig. 17(b) indicates a slightly higher photodegradation of MB dye (~82%) than that reported for CV dye, followed by a slight increase in $C C_0^{-1}$ in the remaining minutes. This is probably due to MB exhibiting stronger electrostatic interactions with negatively charged surfaces and under alkaline conditions ($pH > pH_{ZCP}$), which enhances its degradation [71]. On the other hand, CV dye degradation is seen to be favored at neutral pH (6.8 to 7.0) [72].

Additionally, the apparent kinetic pseudo-first order constant reported for CV and MB dye, in the operational conditions shown in Fig. 14, was $k = 0.0105 \text{ min}^{-1}$ ($R^2 = 0.9418$) and $k = 0.0098 \text{ min}^{-1}$ ($R^2 = 0.9659$), respectively, according to the Langmuir-Hinshelwood model curve fitting. This indicates that while MB undergoes greater overall degradation, CV degrades comparatively faster under the experimental conditions in Fig. 17. The higher rate constant for CV suggests that, kinetically, its degradation occurs more quickly at a given moment, even if its total removal over time is lower. Fig. 18 shows the prediction performed for the bicomponent system in the wavelength of the mixture ($\lambda = 630$ nm) for 240 min.

According to Fig. 18, at 630 nm, ~85% dye degradation is achieved after 180 min, with a slight increase until 240 min. The apparent kinetic pseudo-order constant measured for the binary dye mixture under the conditions of Fig. 15 was carried out was $k = 0.0112 \text{ min}^{-1}$, which was very close to the experimental value, $k = 0.0100 \text{ min}^{-1}$. This result confirms the good accuracy of the ANN-MLP algorithm and the deep learning approach in the degradation reaction progress estimation and in addressing the variables with higher influence in the predictions. Furthermore, this finding proved the suitability of the MLP-ANN algorithm in predicting new data in and beyond the time used in the experimental set. Fig. 19 shows the parity plot constructed for analyzing the relationship between predicted and observed (experimentally) absorbance values to inform the reliability of the developed model.

According to Fig. 19, the developed model demonstrated strong reliability in relating Y_{pred} and Y_{obs} as indicated by the high determination coefficients ($R^2 = 0.9890$ for training and $R^2 = 0.9910$ for testing). These values suggest excellent reproducibility and a strong correlation with experimental data variability.

To investigate the effect of the selected wavelengths on the absorbance reading and prediction, a scan in the visible region ($\lambda = 400$ –700 nm) was carried out for the binary mixture. Thus, Fig. 20 shows the spectrum of organic dyes, individually and in the binary mixture.

According to Fig. 20, in a monocomponent system, CV and MB dyes exhibit maximum light absorption at $\lambda = 590$ nm and 664 nm, respectively. When these dyes are mixed at low concentrations (10 mg L^{-1}), a slight shift in their characteristic wavelengths is observed. However, at higher concentrations (50 mg L^{-1}), the mixture results in a minor shift in the MB absorption peak (from 664 to 663 nm) and the emergence of a new absorption peak at 630 nm. This additional peak may arise from molecular interactions between CV and MB, such as aggregation, complex formation, or changes in the electronic environment due to dye-dye interactions at higher concentrations [73]. For example, studies report

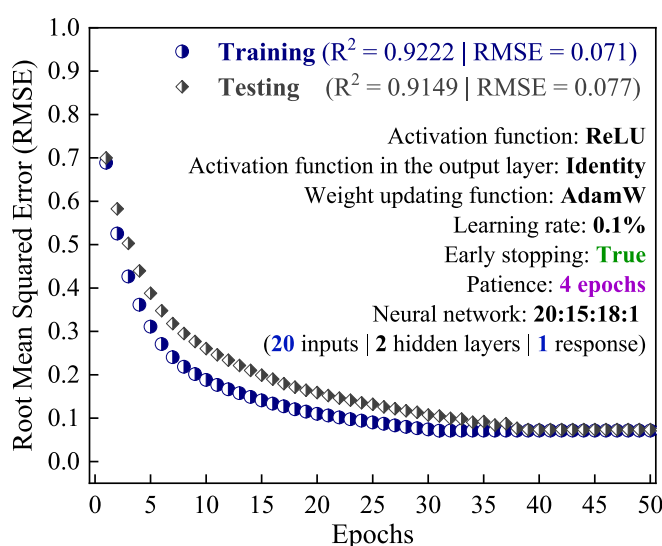


Fig. 16. Learning profile of the MLP-ANN algorithm (optimal configuration).

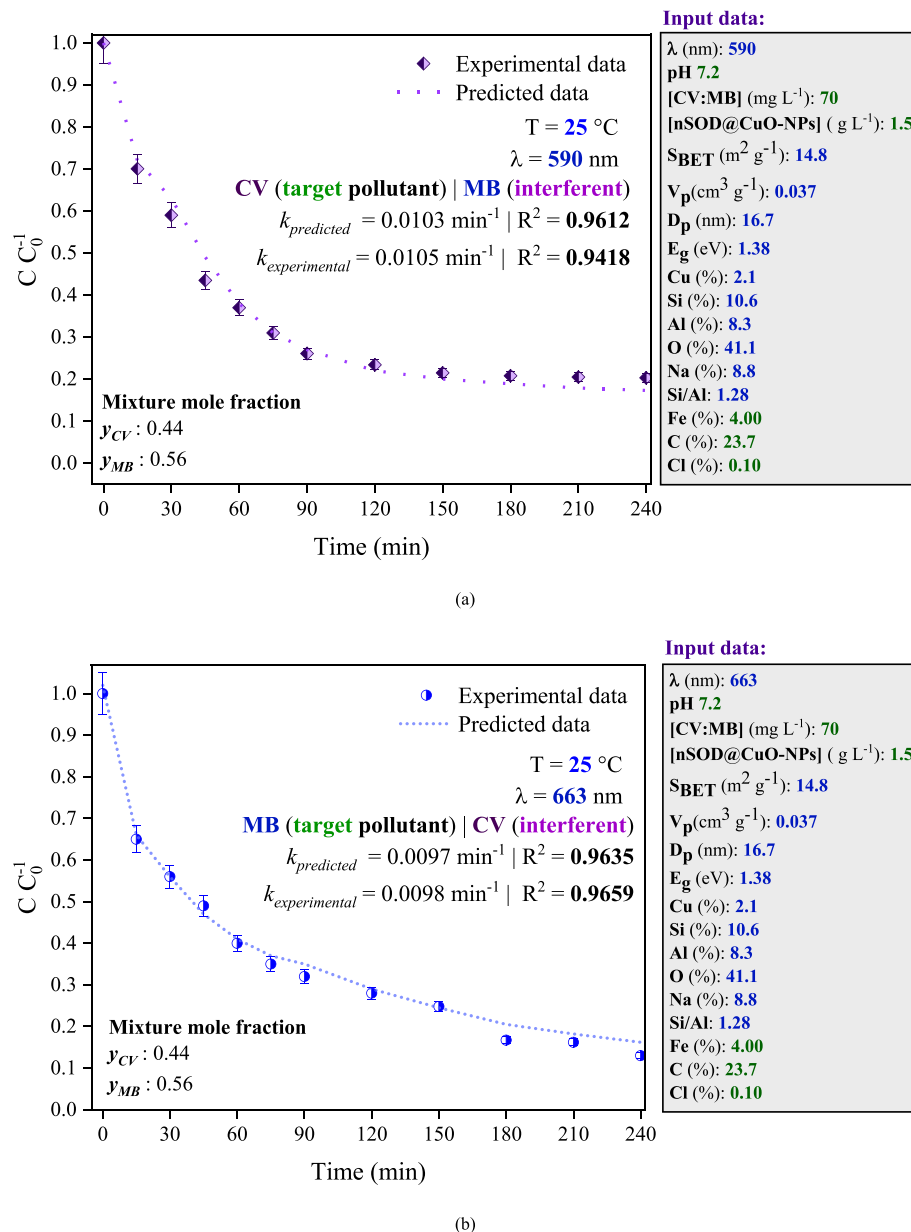


Fig. 17. Prediction of the degradation curve for CV and MB dyes (a) at $\lambda = 590$ nm and (b) at $\lambda = 663$ nm.

that at higher concentrations, dye molecules tend to aggregate due to intermolecular interactions (e.g., π - π stacking or electrostatic forces), leading to new light absorption features [74]. This phenomenon is well-documented for cationic dyes such as MB and CV. The present work used CV:MB dye mixture at concentrations of 50 mg L⁻¹ and higher, thus, the approach used in experimental design and deep learning (absorbance reading at $\lambda = 590$, 630, and 663 nm) shows great coherence with experimental observations reported in the literature. Therefore, this methodology can be used for further studies dealing with crystal violet and methylene blue dyes in bicomponent systems.

3.4. In vitro safety profile

Fig. 21 shows the results of the assays used to evaluate the safety profile of the nanocomposite reinforcement (CuO-NPs) toward the VERO cell lines, carried out on 24, 48, and 72 h.

According to **Fig. 21** and regarding MTT, it was observed a slight increase in cell viability at low concentrations (12.5 and 25 mg L⁻¹) after 24 h, probably due to a proliferative or antioxidant effect of green

tea, whereas in higher concentrations (50 and 100 mg L⁻¹) a reduction of the cell viability was noticeable, suggesting dose-dependent toxicity. At 48 h, cell viability decreases more sharply, especially at concentrations of 50 and 100 mg L⁻¹, indicating a stronger cytotoxic effect with increasing exposure time, possibly related to oxidative stress or induction of apoptosis [75].

After 72 h, cell viability continues to be reduced, although without significant drops compared to 48 h, suggesting that toxicity reaches a plateau, where the most sensitive cells are eliminated and a more resistant population survives [76]. Overall, these results indicate that the toxic effect of CuO-NPs showed temporal and concentration-related dependency, with the greatest impact between 48 and 72 h at higher concentration values. CuO-NPs can induce toxicity in the cells mainly due to ROS generation, which will be discussed later. Moreover, the nature of CuO-NPs (obtained by green synthesis using the green tea extract) may positively influence cell viability at low concentrations, but at higher concentrations, the toxicity of the nanoparticles prevails.

Regarding the production of nitric oxide (NO) in cells treated with CuO-NPs, it was observed that the positive control (C+) showed a

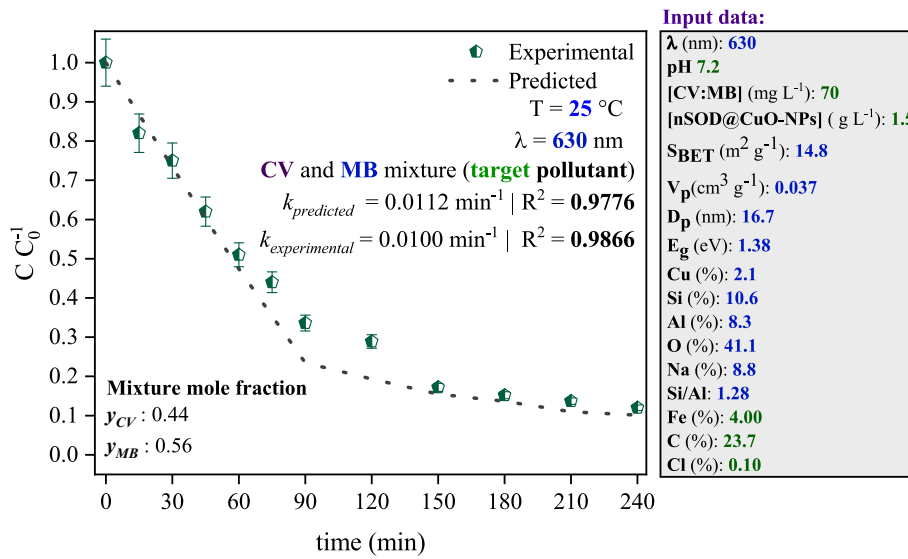


Fig. 18. Prediction of the degradation curve for CV and MB dyes at $\lambda = 630$ nm.

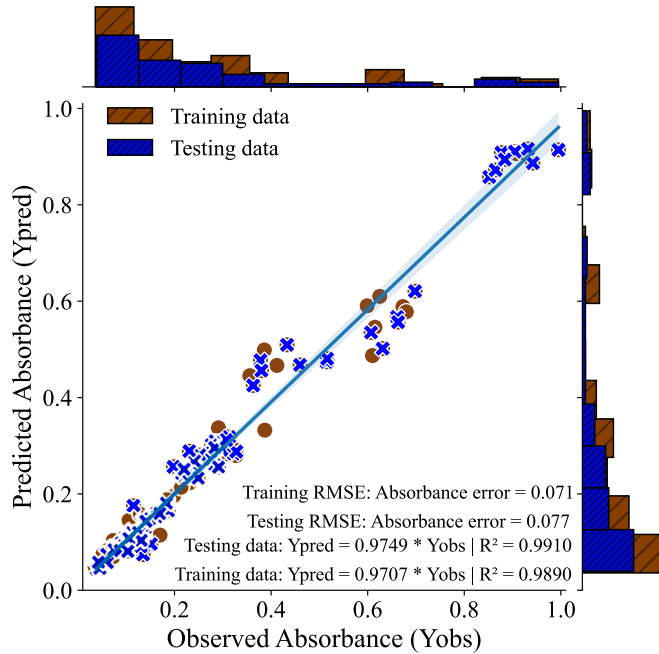


Fig. 19. Parity plot for the developed MLP-ANN algorithm-based model.

significant increase in NO production after 24 h, indicating an intense inflammatory response. However, cells treated with CuO-NPs at different concentrations (12.5–100 mg L⁻¹) demonstrate a marked reduction in NO levels, suggesting that nanoparticles can reduce inflammation [77]. At 48 h, the same pattern is observed, in which the positive control continues to show a significant elevation in NO production, while all concentrations show reduced NO levels, close to the negative control (C-), reinforcing the anti-inflammatory potential of the nanoparticles. At 72 h, the inhibitory effect on NO production by CuO-NPs remains evident, with levels even lower than those of C+, indicating a sustained suppression of the inflammatory response over time. These results suggest that CuO-NPs showed significant anti-inflammatory potential, reducing NO production even in the face of an inflammatory stimulus represented by the positive control. This action can probably be related to the antioxidant properties of green tea, which can modulate inflammatory pathways and reduce oxidative stress [78]. Additional

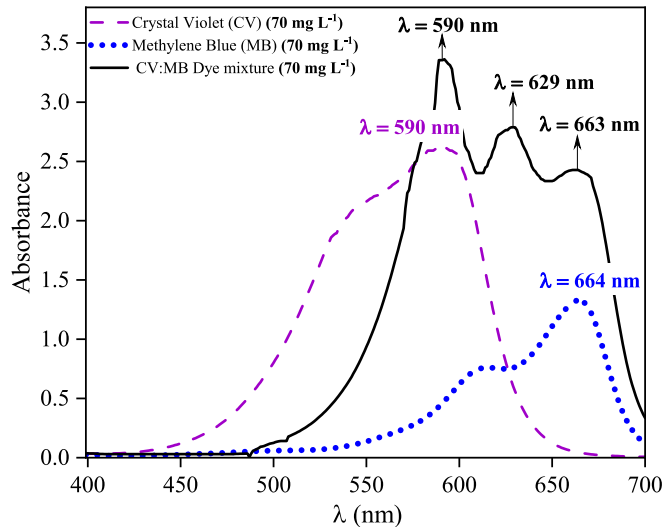


Fig. 20. Spectrum of light absorbance of the organic dyes in the visible radiation region.

studies, such as evaluation of pro-inflammatory mediators and signaling pathways involved, are needed to elucidate the mechanisms of this anti-inflammatory action.

Furthermore, according to Fig. 18, after 24 h, the C+ showed a significant increase in ROS levels, indicating strong oxidative stress. Thus, the cells treated with CuO-NPs show a concentration-dependent increase in ROS production, although lower than C+, suggesting that the nanoparticles can induce a certain degree of oxidative stress, although in a less aggressive manner [79]. At 48 h, ROS levels remain high in the C+, while the treated samples continue to present a dose-dependent increase, with higher concentrations (50 and 100 mg L⁻¹) inducing a significant production of ROS and suggesting that, over time, the oxidative effect of the nanoparticles intensifies. At 72 h, the profile remained similar, with the positive control showing high levels of ROS and the nanoparticles still promoting a significant increase, despite some concentration appearing to show a slight reduction in ROS production compared to previous times. These results indicate that nanoparticles can induce oxidative stress in a moderate and dose-dependent manner, possibly due to the gradual release of copper ions, which promote the generation of free radicals [80]. However, the presence of antioxidant

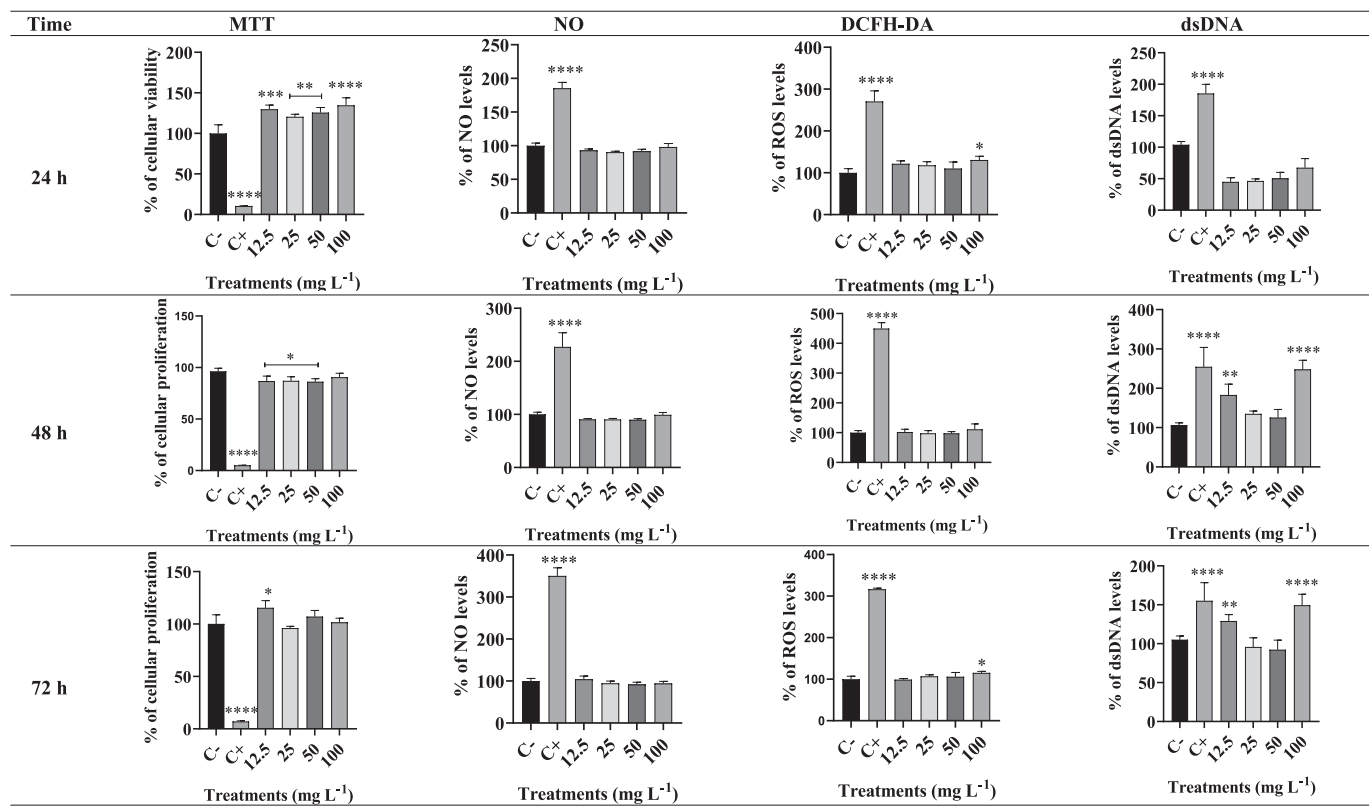


Fig. 21. In vitro safety profile of CuO-NPs at 24, 48, and 72 h in VERO cell line.

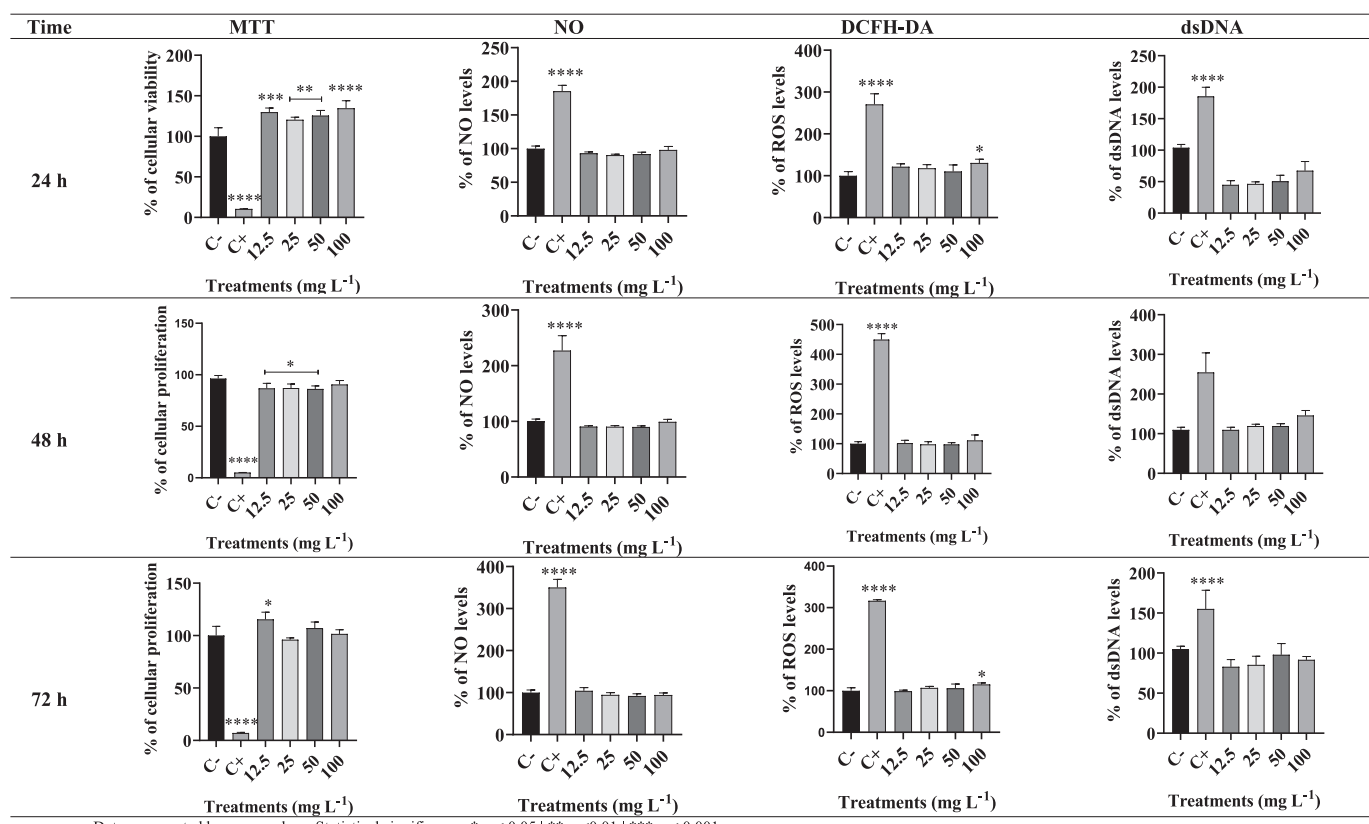


Fig. 22. In vitro safety profile of nSOD at 24, 48, and 72 h in VERO cell line.

compounds in green tea may be attenuating this effect compared to the C+. Additional studies are needed to understand whether the activation of cellular antioxidant defense mechanisms can compensate for this increase in ROS production in the long term.

In relation to the quantification of dsDNA (double-stranded DNA), it was noticeable that after 24 h, a significant increase in the amount of dsDNA was observed, especially at higher concentrations (25 and 50 mg L⁻¹). Thus, this increase may indicate cell proliferation or a stress response, such as an attempt to repair DNA damage. The statistical significance compared to the control group (C-) suggests that the treatment significantly affected the integrity or amount of DNA. After 48 h, there is still an increase in dsDNA at all concentrations, although less pronounced than at 24 h, which may indicate an adaptive response or partial cellular repair. This pattern may also suggest the onset of cytotoxic effects or inhibition of cell proliferation [81]. At 72 h, a significant increase in the amount of dsDNA was observed at the highest concentrations (especially at 50 mg L⁻¹), with clear statistical significance. This result suggests a cumulative cellular response over time, possibly due to prolonged oxidative stress caused by the nanoparticles and/or green tea [82]. Overall, the results indicate that the dsDNA response to treatment is time- and dose-dependent.

Fig. 22 informs the in vitro safety profile carried out for the matrix nanocomposite (nSOD) toward the VERO cell lines, carried out in 24, 48, and 72 h.

According to MTT results at 24 h, the cell viability was maintained at all concentrations tested, with no significant reduction compared to the C-. This suggests that treatment with nSOD does not exert an acute cytotoxic effect during this period and may even have a slight protective effect due to biocompatibility of nanozeolites [83]. After 48 h, a slight reduction in cell viability was observed at the highest concentrations, although the decrease was not as pronounced. This behavior may indicate the onset of cellular stress or adaptation to the nanoparticles, which justifies the presence of statistical significance at some concentrations [84]. At 72 h, the cell viability showed a more evident reduction, especially at the highest concentrations. This pattern suggests a cumulative cytotoxic effect, possibly due to the accumulation of nanoparticles or the depletion of cellular antioxidant defenses [85]. In addition, cellular oxidative stress and mitochondrial dysregulation can contribute to a time-dependent cytotoxic effect [86]. The fact that viability does not drop dramatically even at high concentrations indicates that nSOD has a relatively low toxicity profile, although it can induce moderate cellular stress with prolonged exposure.

Regarding NO generation, after 24 h, the samples treated with nSOD showed low NO production, close to the C- at all concentrations. This observation suggests that nSOD may have an antioxidant or anti-inflammatory effect, inhibiting stress-induced NO generation [61]. After 48 h, NO production remained low and stable in the groups treated with nSOD. This pattern suggests that the nanoparticles can maintain the inhibition of NO production for a prolonged period, possibly due to the antioxidant action of nSOD, which converts superoxide (O₂^{•-}) into hydrogen peroxide (H₂O₂), reducing the substrate required for NO synthesis by cells. Moreover, after 72 h, it was observed that the samples treated with nSOD continued to report low levels of NO, regardless of the concentration used. Thus, the absence of a cumulative increase in NO production suggests that nSOD probably does not induce significant oxidative stress and may have a sustained protective effect over time. The results indicate that nSOD modulates NO production in a concentration-independent manner, maintaining low NO levels even at higher concentrations and for prolonged periods [87]. Similarly, to the hypothesis discussed in the MMT assay, this effect is likely due to the biocompatibility of nSOD to the cells tested, which minimizes oxidative stress and inflammation.

In addition, according to **Fig. 22**, after 24 h, the ROS production was significantly lower in the samples treated with nSOD and was close to the C- at all concentrations tested. This result suggests that nSOD exerts an antioxidant effect, efficiently neutralizing ROS in the first 24 h of

exposure. Additionally, after 48 h, ROS production in the groups treated with nSOD and ROS levels remained low and stable, regardless of the concentration. This indicates that nSOD maintained its biocompatibility over time, preventing the accumulation of ROS in cells. The absence of an increase in ROS production at higher concentrations suggests that the nanoparticles probably do not induce additional oxidative stress and can provide continuous protection against reactive species. At 72 h, ROS production remained low in samples treated with nSOD, similar to the levels observed at 24 and 48 h. This pattern demonstrates that nSOD provides sustained antioxidant protection, preventing ROS accumulation even with prolonged exposure.

Regarding dsDNA levels after 24 h, it was observable that samples treated with nSOD showed dsDNA levels similar to the C- at all concentrations tested, suggesting that the nanoparticles do not cause significant DNA damage during this period. Furthermore, nSOD may protect cells against oxidative DNA damage. After 48 h, in the groups treated with nSOD, dsDNA levels remained low and close to C-, regardless of the concentration. This pattern suggests that the nanoparticles maintain their protective action over time, preventing the accumulation of DNA damage. The absence of dose-dependent variation indicates that the protective effect occurs even at higher concentrations. Additionally, after 72 h, samples treated with nSOD remained with stable dsDNA levels, similar to the negative control. This result suggests that the nSOD does not induce DNA damage even after prolonged exposure. The maintenance of low levels of dsDNA reinforces the hypothesis that nanozeolites may offer sustained protection against oxidative stress and genotoxic damage [88].

Fig. 23 presents the results of the assays used to evaluate the in vitro safety profile of the nanocomposite (nSOD@CuO-NPs) toward the VERO cell lines, carried out in 24, 48, and 72 h.

According to **Fig. 23** and MTT, after 24 h, there was an increase in cell viability at higher concentrations (50 and 100 mg L⁻¹), suggesting that the nanocomposite may present dose-dependent toxicity at initial exposures. However, at lower concentrations (1.25 to 25 mg L⁻¹), cell viability is similar to C-group, indicating good biocompatibility at lower doses. After 48 h, a partial recovery in cell viability is observed, regardless of the concentration used. This observation suggests that the cells can adapt or repair initial damage after prolonged exposure. The absence of significant cytotoxicity at 48 h indicates that the toxic effect observed at 24 h may be transient and related to the initial response to oxidative stress induced by the nanoparticles. After 72 h, cell viability remains stable in the groups treated with nSOD@CuO-NPs. Moreover, there is no significant difference between the concentrations tested, indicating that the nanocomposite does not induce cumulative toxicity over time. The stability in cell viability suggests that the antioxidant properties of nSOD present in the nanocomposite can neutralize the oxidative stress generated by CuO-NPs, contributing to the maintenance of cell viability.

After 24 h, NO production was significantly lower and close to the negative control (C-) at all concentrations tested. This result suggests that the nanocomposite does not stimulate NO production in the first 24 h and may have a modulating effect on the initial inflammatory response. After 48 h, NO levels remained low and stable, regardless of the concentration used. This suggests that the nanocomposite maintains its modulating action over time, preventing the accumulation of NO in cells. The absence of an increase in NO production at higher concentrations suggests that nSOD@CuO-NPs may not induce a significant inflammatory response and may exert a protective effect against nitrosative stress. At 72 h, NO production remained low and constant, similar to the levels observed at 24 and 48 h. This pattern indicates that the nanocomposite provides a sustained anti-inflammatory effect, neutralizing excessive NO production even with prolonged exposure.

Moreover, **Fig. 23** reports the results of ROS generation, measured by the DCF (dichlorofluorescein) assay, after treatments with the nSOD@CuO-NPs nanocomposite at different concentrations (12.5–100 mg L⁻¹) and exposure times (24, 48, and 72 h). Thus, after 24 h, there is

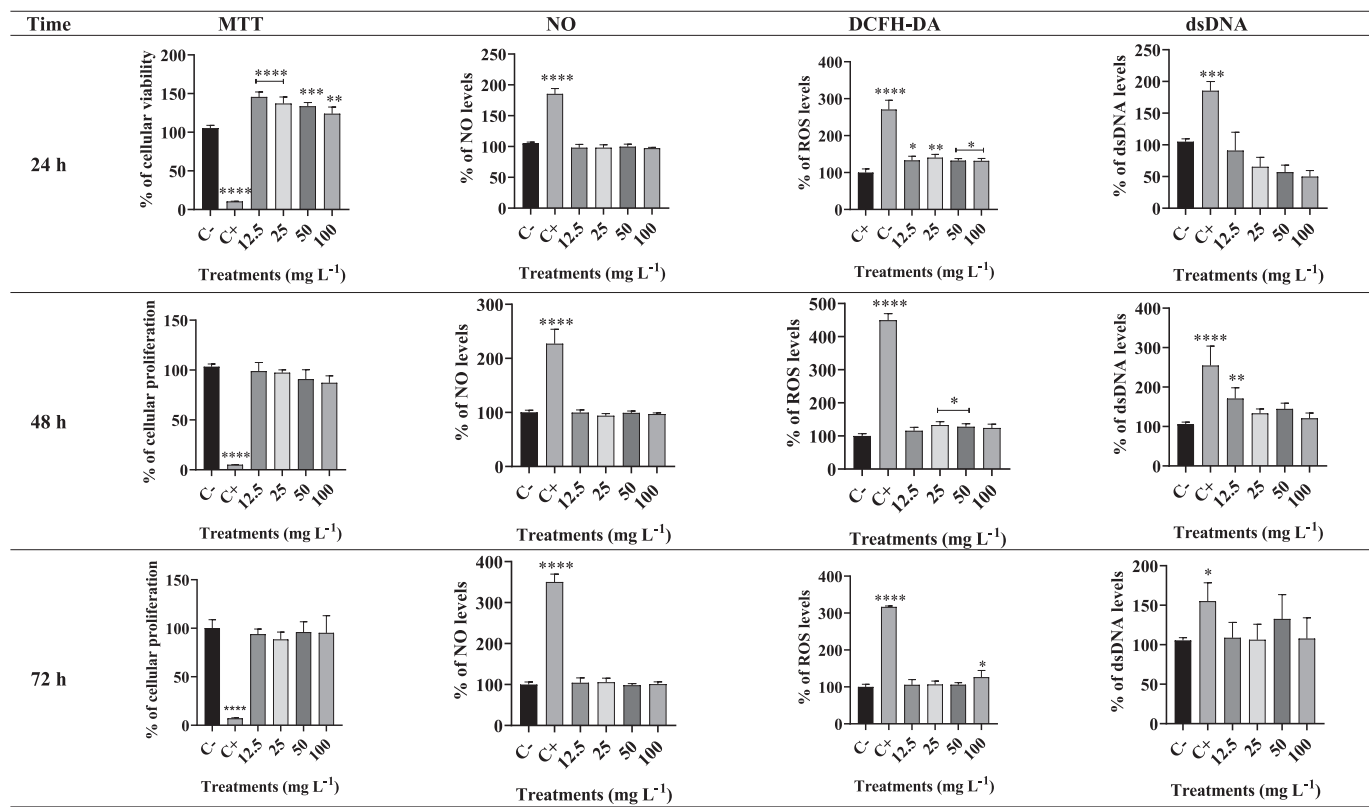


Fig. 23. In vitro safety profile of nSOD@CuO-NPs at 24, 48, and 72 h in VERO cell line.

a significant reduction in ROS production at all concentrations tested when compared to C+. This result suggests that the nanocomposite exerts an antioxidant effect, neutralizing the initial oxidative stress. After 48 h, a maintenance of low ROS levels is observed. This indicates that the antioxidant effect of the nanocomposite is sustained over time. Notably, at lower concentrations (1.25 and 5 mg L⁻¹), ROS levels remain close to the C-, suggesting high antioxidant efficacy even at reduced doses. Additionally, at higher concentrations (50 and 100 mg L⁻¹), there is a slight increase in ROS production, although it is not statistically significant in relation to the negative control. This may indicate that high doses of the nanocomposite can generate a mild oxidative response, possibly due to the presence of CuO-NPs [89]. At 72 h, the groups treated with nSOD@CuO-NPs maintained low and stable levels of ROS. There is no significant difference between the concentrations tested, suggesting that the nanocomposite may not induce cumulative oxidative stress. The stability in ROS levels over time suggests that the antioxidant effect of nSOD is long-lasting, providing continuous protection against oxidative stress.

Regarding dsDNA using PicoGreen® reagent, Fig. 23 reports the results that evaluate the integrity and quantity of DNA, which is an indicator of cytotoxicity and genetic damage. Thus, after 24 h, there is a significant reduction in the amount of dsDNA at all concentrations, when compared to the C+. This result suggests that the nanocomposite exerts a protective effect against DNA damage. Some antioxidant action of nSOD may be neutralizing ROS, which is responsible for causing DNA strand breaks. After 48 h, there was a stabilization in the amount of dsDNA, maintaining levels close to the C-. This indicates that the protective effect of the nanocomposite is sustained over time, preventing cumulative DNA damage [90]. The lower concentrations (1.25 and 50 mg L⁻¹) were equally effective as the higher concentrations, indicating that lower doses are sufficient to achieve the protective effect. Moreover, after 72 h, the groups treated with nSOD@CuO-NPs maintained stable and low levels of dsDNA, similar to the C-. There was no significant

difference between the concentrations tested, indicating that the nanocomposite does not cause DNA damage even at high doses or in prolonged exposure. This genotoxic safety profile reinforces the potential of nSOD@CuO-NPs as a safe antioxidant for biological use.

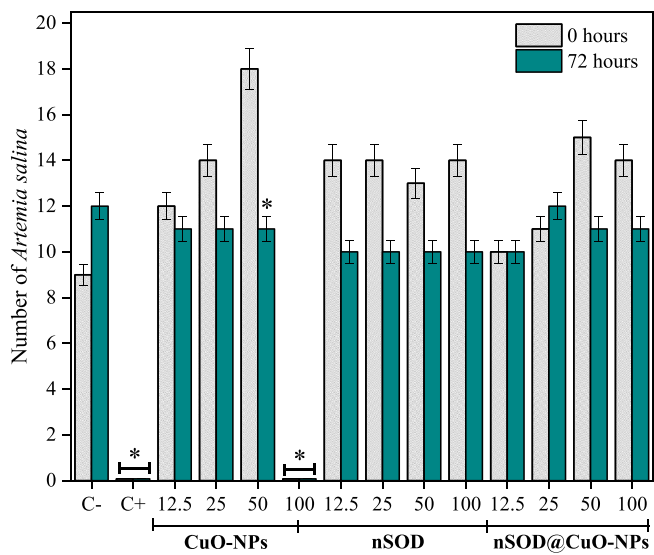
3.5. Ecotoxicity

The following results, Figs. 24(a) and 24(b), demonstrate the acute toxicity effects on *A. salina*. An inverse relationship was observed between the number of *A. salina* nauplii and the number of hatched eggs. This pattern suggests that under toxic conditions, *A. salina* may produce more eggs as a defense mechanism to ensure population survival, reducing the immediate number of nauplii due to the energy allocation toward egg production [91].

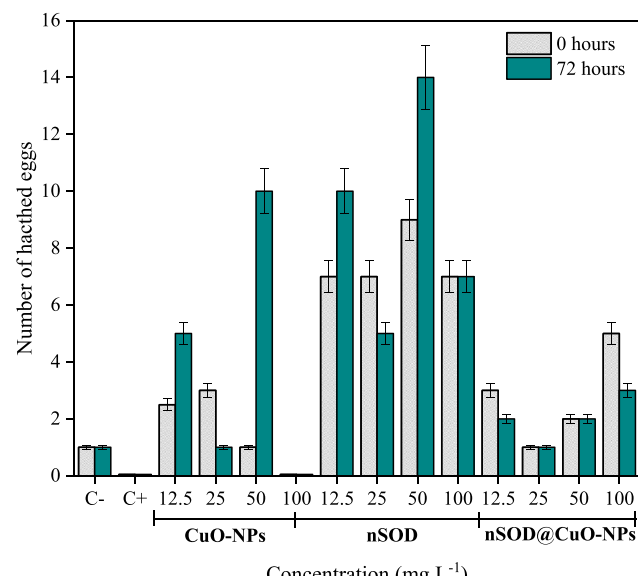
According to Fig. 24, the exposure of *A. salina* to CuO-NPs significantly reduced the number of *A. salina* nauplii developed over 72 h at higher concentrations ($p < 0.05$). This reduction aligns with the high mortality observed in Fig. 24(a), probably due to oxidative stress and Cu²⁺ ion release, which can interfere with normal embryonic development, disrupt metabolic activity, and impair hatching. The most severe inhibition occurred at 100 mg L⁻¹ (the lethal copper concentration), confirming the acute developmental toxicity of CuO-NPs.

In contrast, exposure of *A. salina* to nSOD led to an increase in the number of nauplii compared to the control, suggesting that the sodalite nanozeolite may create a more favorable environment for egg development. Since nSOD does not release toxic metal ions or induce oxidative stress, its high surface area and ion-exchange capacity could improve water quality and enhance the survival and reproduction of *A. salina*. Importantly, no statistically significant difference ($p > 0.05$) was observed between nSOD-treated groups and the C- group, reinforcing its biocompatibility.

Similarly, the nSOD@CuO-NPs nanocomposite resulted in an increase in nauplii development compared to CuO-NPs alone, though not



(a)



(b)

Fig. 24. Ecotoxicity of CuO-NPs, nSOD, and nSOD@CuO-NPs in terms of (a) number of *A. salina* survived and (b) number of *A. salina* eggs hatched after nanoparticles exposure.

as pronounced as in the nSOD group. This suggests that the sodalite matrix mitigates CuO-NPs toxicity by controlling Cu^{2+} release and limiting oxidative stress, thereby preventing severe developmental inhibition [92]. However, at the highest concentration, a slight but statistically significant decrease ($p < 0.05$) in nauplii development was observed compared to the control, indicating that some residual toxicity remains. Therefore, these findings suggest that while CuO-NPs impair *A. salina* development, nSOD enhances egg viability, and its incorporation into the nanocomposite reduces the toxic effects of CuO-NPs, probably due to a controlled release mechanism that limits metal ion exposure and oxidative damage.

4. Conclusion

In this work, a novel copper/nanozeolite-based nanocatalyst (nSOD@CuO-NPs) was synthesized using (agro)industrial waste and *Camellia sinensis* extract. The nSOD@CuO-NPs exhibited good physicochemical stability ($ZP = -18.5 \pm 1.0 \text{ mV}$), favorable textural properties ($S_{\text{BET}} = 14.8 \pm 0.7$, $V_p = 0.04 \pm 0.001 \text{ cm}^3 \text{ g}^{-1}$, $D_p = 16.7 \pm 0.7 \text{ nm}$), and desirable optical properties ($E_g = 1.38 \text{ eV}$). XRD analysis confirmed the presence of tenorite/cuprite (Cu_2O , CuO) and analcime/sodalite (ANA, SOD) crystalline phases, whereas ATR-FTIR spectra identified T-O-T and O-T-O functional groups (with T = Al or Si). The nanocatalyst exhibited a zero charge point (pH_{ZCP}) at pH 7.65 and the following elemental composition: C (23.7%), O (41.1%), Si (10.6%), Na (8.8%), Al (8.4%), Fe (4.0%), Cu (2.1%). According to the CCRD 2^3 , the photocatalytic degradation efficiency reached 79.4% for CV dye ($k = 0.0105 \text{ min}^{-1}$, $\lambda = 590 \text{ nm}$), 82.9% for MB dye ($k = 0.0098 \text{ min}^{-1}$, $\lambda = 663 \text{ nm}$), and 84.5% for binary dye mixture ($k = 0.0108 \text{ min}^{-1}$, $\lambda = 630 \text{ nm}$) under optimal conditions (pH 10, $[\text{CV:MB}] = 70 \text{ mg L}^{-1}$, $[\text{nSOD@CuO-NPs}] = 1.5 \text{ g L}^{-1}$). Deep learning analysis identified 18 significant variables influencing the photocatalytic degradation of CV and MB dyes in the binary mixture. The algorithm successfully predicted absorbance readings and degradation profiles at $\lambda = 590$, 630, and 663 nm, demonstrating its applicability in assessing the degradation of persistent organic pollutants under visible light radiation. The MLP-ANN algorithm exhibited good predictive performance ($R_{\text{training}}^2 = 0.9149$, $R_{\text{test}}^2 = 0.9222$ / $\text{RMSE}_{\text{training}} = 0.071$, $\text{RMSE}_{\text{test}} = 0.077$) with a 20:15:18:1 neural network architecture. The model predicted 79–84% and 82–88% dye degradation at 180 and 240 min, respectively, which closely aligned with experimental results. These findings confirm that deep learning can be effectively used to predict dye absorbance and photocatalytic degradation profile over time, emphasizing the role of artificial intelligence in the design and optimization of advanced oxidation processes (AOPs) for organic pollutant removal in bicomponent systems and under visible radiation. According to cytotoxicity assays, incorporating CuO-NPs into nSOD maintained cellular viability (120 to 100% between 24 and 72 h), preserved ROS levels, and reduced damage in VERO cells after 72 h, probably by mitigating DNA damage and oxidative stress. Regarding ecotoxicity, nSOD@CuO-NPs reduced acute toxicity toward *A. salina* after 72 h, in contrast to CuO-NPs, which exhibited a lethal effect at 100 mg L^{-1} . Furthermore, correlating the potential application of deep learning to bioactivity modeling is a promising future challenge, as this modeling is based on the interaction of a specific molecule with a biological target, such as a cell line, and predicting the desired effect. Traditionally, this process relies on high-throughput experiments and simple computational models, which often fail to capture the complexity of molecular interactions. Deep learning changes this scenario by allowing models and deep neural networks to learn complex patterns directly from data, rather than relying on predefined molecular characteristics. This allows them to automatically identify the most relevant characteristics for predicting bioactivity, helping to unravel the complexity of life at the molecular level. In summary, the synthesized nanocomposite demonstrated promising photocatalytic performance and a favorable in vitro safety profile, while deep learning proved to be a powerful tool for predicting photocatalytic reaction progress in AOPs under visible radiation.

CRediT authorship contribution statement

Leandro Rodrigues Oviedo: Writing – review & editing, Writing – original draft, Validation, Methodology, Investigation, Formal analysis, Data curation, Conceptualization. **Daniel Moro Druzian:** Writing – review & editing, Validation, Methodology, Investigation, Formal analysis, Data curation. **Sthefany Nunes Loureiro:** Writing – review & editing, Validation, Investigation, Formal analysis, Data curation. **Alencar Kolinski Machado:** Writing – review & editing, Validation, Supervision, Investigation, Formal analysis, Data curation. **Taíse**

Regina Schuster Montagner: Writing – review & editing, Validation, Methodology, Investigation, Formal analysis, Data curation. **Giovani Pavoski:** Writing – review & editing, Methodology, Investigation, Formal analysis, Data curation. **Denise Crocce Romano Espinosa:** Writing – review & editing, Validation, Supervision, Methodology, Formal analysis, Data curation. **Yolice Patricia Moreno Ruiz:** Writing – review & editing, Validation, Supervision, Methodology, Formal analysis, Data curation. **Lissandro Dorneles Dalla Nora:** Writing – review & editing, Supervision, Investigation, Formal analysis, Data curation. **William Leonardo da Silva:** Writing – review & editing, Writing – original draft, Validation, Supervision, Investigation, Formal analysis, Data curation, Conceptualization.

Declaration of competing interest

The authors declare that they have no known competing financial interests or personal relationships that could have appeared to influence the work reported in this paper.

Acknowledgements

Authors would also like to thank Department of Fundamental Chemistry (DQF), LAREX (USP, Brazil-SP) and Franciscan University for instrumental support. This study was financed by the CAPES (Coordination of Superior Level Staff Improvement) - Finance Code 001.

Appendix A. Supplementary data

Supplementary data to this article can be found online at <https://doi.org/10.1016/j.molliq.2025.128403>.

Data availability

The data that support the findings of this study are available on request from the corresponding author.

References

- [1] H.R. Dihom, M.M. Al-Shaibani, R.M.S. Radin Mohamed, A.A. Al-Gheethi, A. Sharma, M.H.B. Khamidun, Photocatalytic degradation of disperse azo dyes in textile wastewater using green zinc oxide nanoparticles synthesized in plant extract: A critical review, *J Water Process Eng* 47 (2022) 102705–102716, <https://doi.org/10.1016/j.jwpe.2022.102705>.
- [2] R. Al-Tohamy, S.S. Ali, F. Li, K.M. Okasha, Y.A.-G. Mahmoud, T. Elsamahy, H. Jiao, Y. Fu, J. Sun, A critical review on the treatment of dye-containing wastewater: ecotoxicological and health concerns of textile dyes and possible remediation approaches for environmental safety, *Ecotoxicol. Environ. Saf.* 231 (2022) 113160–113177, <https://doi.org/10.1016/j.ecoenv.2021.113160>.
- [3] D. Olivo-Alanís, A. García-González, M.A. Mueses, R.B. García-Reyes, Generalized kinetic model for the photocatalytic degradation processes: validation for dye wastewater treatment in a visible-LED tubular reactor, *Appl. Catal. B Environ.* 317 (2022) 121804–121815, <https://doi.org/10.1016/j.apcatb.2022.121804>.
- [4] S. Mohd, A.M. Khan, Heterogeneous photocatalysis: Recent advances and applications, in: M. Sen (Ed.), Sustainable Green Catalytic Processes, 1st ed, Wiley, 2024, pp. 141–163, <https://doi.org/10.1002/9781394212767.ch7>.
- [5] F. Soori, A. Nezamzadeh-Ejhieh, Synergistic effects of copper oxide-zeolite nanoparticles composite on photocatalytic degradation of 2,6-dimethylphenol aqueous solution, *J. Mol. Liq.* 255 (2018) 250–256, <https://doi.org/10.1016/j.molliq.2018.01.169>.
- [6] C. Bharathi, R. Rajeswari, P. Janaki, A.P. Sivamurugan, G.K. Senthil, S. Radhamani, R. Sathy Priya, M. Sangeetha, S. Thenmozhi, N. Chiranjeevirajan, R. Sharmila, B. Ramya, R. Balamurugan, Bio-mediated synthesis of nanoparticles: A new paradigm for environmental sustainability, *Plant Sci. Today* 12 (2025) 1–13, <https://doi.org/10.14719/pst.5192>.
- [7] I. Khaldari, M.R. Naghavi, E. Motamed, Synthesis of green and pure copper oxide nanoparticles using two plant resources via solid-state route and their phytotoxicity assessment, *RSC Adv.* 11 (2021) 3346–3353, <https://doi.org/10.1039/DORA09924D>.
- [8] M.N. Kumar, C.S. Rahale, H. Shanmugam, K. Vanitha, N. Saranya, M. Prasantha Rajan, Eco-friendly synthesis of zinc oxide nanoparticles using *Camellia sinensis* (green tea) and its characterization, *IJPSS* 35 (2023) 56–61, <https://doi.org/10.9734/ijpss/2023/v35i203785>.
- [9] S. Mintova, M. Jaber, V. Valtchev, Nanosized microporous crystals: emerging applications, *Chem. Soc. Rev.* 44 (2015) 7207–7233, <https://doi.org/10.1039/C5CS00210A>.
- [10] H. Guo, L. Zhao, C. Martineau-Corcos, F. Fayon, J. Viger-Gravel, H. Awala, P. Boullay, J. Grand, A. Vicente, J. Gilson, S. Mintova, Transformation of discrete amorphous aluminosilicate nanoparticles into nanosized zeolites, *Adv. Materials. Inter.* 8 (2021) 2000634–2000646, <https://doi.org/10.1002/admi.202000634>.
- [11] E.A. Abdelrahman, Y.G. Abou El-Reash, H.M. Youssef, Y.H. Kotp, R.M. Hegazey, Utilization of rice husk and waste aluminum cans for the synthesis of some nanosized zeolite, zeolite/zeolite, and geopolymers/zeolite products for the efficient removal of Co(II), Cu(II), and Zn(II) ions from aqueous media, *J. Hazard. Mater.* 401 (2021) 123813–123822, <https://doi.org/10.1016/j.jhazmat.2020.123813>.
- [12] M. Yoldi, E.G. Fuentes-Ordoñez, S.A. Korili, A. Gil, Zeolite synthesis from industrial wastes, *Microporous Mesoporous Mater.* 287 (2019) 183–192, <https://doi.org/10.1016/j.micromeso.2019.06.009>.
- [13] A. Nezamzadeh-Ejhieh, M. Karimi-Shamsabadi, Comparison of photocatalytic efficiency of supported CuO onto micro and nano particles of zeolite X in photodecolorization of methylene blue and methyl orange aqueous mixture, *Appl. Catal. A Gen.* 477 (2014) 83–92, <https://doi.org/10.1016/j.apcata.2014.02.031>.
- [14] I. Khan, I. Khan, M. Usman, M. Imran, K. Saeed, Nanoclay-mediated photocatalytic activity enhancement of copper oxide nanoparticles for enhanced methyl orange photodegradation, *J. Mater. Sci. Mater. Electron.* 31 (2020) 8971–8985, <https://doi.org/10.1007/s10854-020-03431-6>.
- [15] H. Koohestani, H. Mansouri, A. Pirmoradian, M. Hassanabadi, Investigation of photocatalytic efficiency of supported CuO nanoparticles on natural zeolite particles in photodegradation of methyl Orange, *J. Nanosci. Nanotechnol.* 20 (2020) 5964–5969, <https://doi.org/10.1166/jnn.2020.18548>.
- [16] M. Bahramian, R.K. Dereli, W. Zhao, M. Giberti, E. Casey, Data to intelligence: the role of data-driven models in wastewater treatment, *Expert Syst. Appl.* 217 (2023) 119453–119464, <https://doi.org/10.1016/j.eswa.2022.119453>.
- [17] M.D.C.R. Da Silva, D.M. Druzian, L.F.W. Brum, C. Dos Santos, G. Pavoski, D.C. R. Espinosa, Y.P.M. Ruiz, A. Galembeck, W.L. Da Silva, Green synthesis of ZrO₂/PdO-NPs for photodegradation of anionic dyes: photocatalytic activity and machine learning modelling, *J. Mol. Liq.* 410 (2024) 125581–125591, <https://doi.org/10.1016/j.molliq.2024.125581>.
- [18] L.R. Oviedo, D.M. Druzian, L.D.D. Nora, W.L. Da Silva, Study of machine learning on the photocatalytic activity of a novel nanozeolite for the application in the rhodamine B dye degradation, *Catal. Today* 443 (2025) 114986–115004, <https://doi.org/10.1016/j.cattod.2024.114986>.
- [19] M.A. Tony, Zeolite-based adsorbent from alum sludge residue for textile wastewater treatment, *Int. J. Environ. Sci. Technol.* 17 (2020) 2485–2498, <https://doi.org/10.1007/s13762-020-02646-8>.
- [20] V.R. Oviedo, D.M. Druzian, S.R. Mortari, M.R. Sagrillo, T.M. Volkmer, D.A. Bertuol, L.F. Rodrigues Jr., Synthesis and characterization of SrO-containing bioglass-ceramic from rice husk silicon dioxide, *Cerámica* 66 (2020) 426–432, <https://doi.org/10.1590/0366-69132020663802979>.
- [21] L.R. Oviedo, P.C.L. Muraro, G. Pavoski, D.C.R. Espinosa, Y.P.M. Ruiz, A. Galembeck, C.R.B. Rhoden, W.L. Da Silva, Synthesis and characterization of nanozeolite from (agro)industrial waste for application in heterogeneous photocatalysis, *Environ. Sci. Pollut. Res.* 29 (2022) 3794–3807, <https://doi.org/10.1007/s11356-021-15815-0>.
- [22] J. Emima Jerónima, L. Allwin Joseph, P. Annie Vinosa, A. Jerline Mary, S. Jerome Das, *Camellia sinensis* leaf extract mediated synthesis of copper oxide nanostructures for potential biomedical applications, *Mater. Today Proc.* 8 (2019) 214–222, <https://doi.org/10.1016/j.matpr.2019.02.103>.
- [23] A. Nezamzadeh-Ejhieh, S. Hushmand, Solar photodecolorization of methylene blue by CuO/X zeolite as a heterogeneous catalyst, *Appl. Catal. A Gen.* 388 (2010) 149–159, <https://doi.org/10.1016/j.apcata.2010.08.042>.
- [24] L.R. Oviedo, D.M. Druzian, G.E. Montagner, Y.P.M. Ruiz, A. Galembeck, G. Pavoski, D.C.R. Espinosa, L.D. Dalla Nora, W.L. Da Silva, Supported heterogeneous catalyst of the copper oxide nanoparticles and nanozeolite for binary dyes mixture degradation: machine learning and experimental design, *J. Mol. Liq.* 402 (2024) 124763–124770, <https://doi.org/10.1016/j.molliq.2024.124763>.
- [25] S. Tabassum, Md. Sahadat Hossain, D. Islam, S. Ahmed, Synthesis of nanocrystallite β-Bi₂O₃ as a photocatalyst through solid-state method for a sturdy treatment of pharmaceutical waste, *Results Surf Interfaces* 18 (2025) 100371–100384, <https://doi.org/10.1016/j.rsurfi.2024.100371>.
- [26] A. Altmann, L. Tolosi, O. Sander, T. Langauer, Permutation importance: a corrected feature importance measure, *Bioinformatic* 26 (2010) 1340–1347, <https://doi.org/10.1093/bioinformatics/btq134>.
- [27] A. El Bey, M. Laidi, A. Yetto, S. Hanini, A. Ibrir, M. Hentabli, H. Ouldkaoua, Practical artificial neural network tool for predicting the competitive adsorption of dyes on Gemini polymeric nanoarchitecture, *Kem. Ind.* 70 (2021) 481–488, <https://doi.org/10.15255/KUI.2020.069>.
- [28] L. Leng, L. Yang, X. Lei, W. Zhang, Z.A.Z. Yang, H. Zhan, J. Yang, X. Yuan, H. Peng, H. Li, Machine learning predicting and engineering the yield, N content, and specific surface area of biochar derived from pyrolysis of biomass, *Biochar* 4 (2022) 63–81, <https://doi.org/10.1007/s42773-022-00183-w>.
- [29] L.D. Soltau Missio Pinheiro, N.Z. Sentena, G.G. Sangui, B.S. Vizzotto, E. De Oliveira Pinto, G. Pavoski, D.C. Romano Espinosa, A.K. Machado, W. Leonardo Da Silva, Copper nanoparticles from acid ascorbic: biosynthesis, characterization, in vitro safety profile and antimicrobial activity, *Mater. Chem. Phys.* 307 (2023) 128110–128119, <https://doi.org/10.1016/j.matchemphys.2023.128110>.

- [30] M.F.B. Da Costa, A.B. Libório, F. Teles, C.D.S. Martins, P.M.G. Soares, G. C. Meneses, F.A.D.P. Rodrigues, L.K.A.M. Leal, D. Miron, A.H. Silva, A.M. C. Martins, Red propolis ameliorates ischemic-reperfusion acute kidney injury, *Phytomedicine* 22 (2015) 787–795, <https://doi.org/10.1016/j.phymed.2015.03.017>.
- [31] W.-S. Choi, P.-G. Shin, J.-H. Lee, G.-D. Kim, The regulatory effect of veratric acid on NO production in LPS-stimulated RAW264.7 macrophage cells, *Cell. Immunol.* 280 (2012) 164–170, <https://doi.org/10.1016/j.cellimm.2012.12.007>.
- [32] P.C. Gölter, J.M. Haro-Moreno, F. Rodriguez-Valera, M.J. Loessner, E. Gómez-Sanz, Uncovering a hidden diversity: optimized protocols for the extraction of dsDNA bacteriophages from soil, *Microbiome* 8 (2020) 17–33, <https://doi.org/10.1186/s40168-020-0795-2>.
- [33] D. Moro Druzian, L. Rodrigues Oviedo, S. Nunes Loureiro, R. Dias Wouters, B. Stefanello Vizzotto, E. De Oliveira Pinto, N. Julia Schüssler De Vanconcellos, Y. Patricia Moreno Ruiz, A. Galembeck, G. Pavoski, D. Crocce Romano Espinosa, C. Dos Santos, W. Leonardo Da Silva, Cerium oxide nanoparticles: biosynthesis, characterization, antimicrobial, ecotoxicity and photocatalytic activity, *Photochem. Photobiol. A: Chem.* 442 (2023) 114773–114785, <https://doi.org/10.1016/j.jphotochem.2023.114773>.
- [34] G. Saha, N. Chandrasekaran, A combined toxicological impact on *Artemia salina* caused by the presence of dust particles, microplastics from cosmetics, and paracetamol, *Environ. Pollut.* 348 (2024) 123822–123834, <https://doi.org/10.1016/j.envpol.2024.123822>.
- [35] O. Ben Messaoud, A. Ouahab, S. Rahmene, S. Hettal, A. Kater, M. Sayad, H. Attouche, N. Gherraf, Optoelectronic and dielectric properties of tenorite CuO thin films sprayed at various molar concentrations, *Period. Polym. Chem. Eng.* 68 (2024) 93–105, <https://doi.org/10.3311/PPch.22136>.
- [36] M.R. Quirino, G.L. Lucena, J.A. Medeiros, I.M.G.D. Santos, M.J.C.D. Oliveira, CuO rapid synthesis with different morphologies by the microwave hydrothermal method, *Mater. Res.* 21 (2018) 1–9, <https://doi.org/10.1590/1980-5373-mr-2018-0227>.
- [37] A.B.D. Nandyanto, R. Zaen, R. Oktiani, Correlation between crystallite size and photocatalytic performance of micrometer-sized monoclinic WO_3 particles, *Arab. J. Chem.* 13 (2020) 1283–1296, <https://doi.org/10.1016/j.arabjc.2017.10.010>.
- [38] L. Garces, Selective N,N-methylation of aniline over cocrystallized zeolites RHO and zeolite X (FAU) and over Linde type L (Sr,K-LTL), *J. Catal.* 217 (2003) 107–116, [https://doi.org/10.1016/S0021-9517\(03\)00048-4](https://doi.org/10.1016/S0021-9517(03)00048-4).
- [39] L. Ahmadpour-Mobarakeh, A. Nezamzadeh-Ejhieh, A zeolite modified carbon paste electrode as useful sensor for voltammetric determination of acetaminophen, *Mater. Sci. Eng. C* 49 (2015) 493–499, <https://doi.org/10.1016/j.msec.2015.01.028>.
- [40] E.C. Paris, J.O.D. Malafatti, A.J. Moreira, L.C. Santos, C.R. Sciena, A. Zenatti, M. T. Escote, V.R. Mastelaro, M.R. Joya, CuO nanoparticles decorated on hydroxyapatite/ferrite magnetic support: photocatalysis, cytotoxicity, and antimicrobial response, *Environ. Sci. Pollut. Res.* 29 (2022) 41505–41519, <https://doi.org/10.1007/s11356-021-18263-y>.
- [41] J. Xie, Y. He, J. Tang, Y. Wang, M. Chamas, H. Wang, Pore size distribution dependent controlling selective degradation of binary dye effluent, *J. Mol. Liq.* 250 (2018) 388–395, <https://doi.org/10.1016/j.molliq.2017.12.029>.
- [42] S. Wu, Y. Li, T. Wang, H. Li, X. Wang, L. Ma, N. Zhang, P. Yue, Y. Li, Design and synthesis of dual functional porphyrin-based COFs as highly selective adsorbent and photocatalyst, *Chem. Eng. J.* 470 (2023) 144135–144144, <https://doi.org/10.1016/j.cej.2023.144135>.
- [43] J.M. Berg, A. Romoser, N. Banerjee, R. Zebda, C.M. Sayes, The relationship between pH and zeta potential of ~ 30 nm metal oxide nanoparticle suspensions relevant to in vitro toxicological evaluations, *Nanotoxicology* 3 (2009) 276–283, <https://doi.org/10.3109/17435390903276941>.
- [44] M. Zain, K.A. Yasin, S. Haq, W. Rehman, S.U. Din, S. Shujaat, A. Syed, M. K. Hossain, B.A. Paray, J. Razzakov, A. Samad, Effect of calcination temperature induced structural modifications on the photocatalytic efficacy of $\text{Fe}_2\text{O}_3\text{-ZrO}_2$ nanostructures: mechanochemical synthesis, *RSC Adv.* 14 (2024) 15085–15094, <https://doi.org/10.1039/d4ra01944j>.
- [45] G. Di Liberto, F. Maleki, G. Pacchioni, pH dependence of MgO , TiO_2 , and $\gamma\text{-Al}_2\text{O}_3$ surface chemistry from first principles, *J. Phys. Chem. C* 126 (2022) 10216–10223, <https://doi.org/10.1021/acs.jpcc.2c02289>.
- [46] A. Clavier, M. Seijo, F. Carnal, S. Stoll, Surface charging behavior of nanoparticles by considering site distribution and density, dielectric constant and pH changes – a Monte Carlo approach, *Phys. Chem. Chem. Phys.* 17 (2015) 4346–4353, <https://doi.org/10.1039/C4CP04733H>.
- [47] S. Salimkhani, K. Siahcheshm, A. Kadkhodaie, H. Salimkhani, Structural analysis and the effect of the chromium on LTA (Na) zeolite synthesized from kaolin, *Mater. Chem. Phys.* 271 (2021) 124957–124967, <https://doi.org/10.1016/j.matchemphys.2021.124957>.
- [48] K.M. Klima, K. Schollbach, H.J.H. Brouwers, Q. Yu, Enhancing the thermal performance of class F fly ash-based geopolymers by sodalite, *Constr. Build. Mater.* 314 (2022) 125574–125587, <https://doi.org/10.1016/j.conbuildmat.2021.125574>.
- [49] N. Zouhri, M. El Amrani, M. Taky, M. Hafsi, A. Elmidaoui, Effectiveness of treatment of water surface with ferric chloride and aluminium sulphate, *Rev. Catal.* 2 (2015) 1–13, <https://doi.org/10.18488/journal.96.2015.2.1/96.1.1.13>.
- [50] Y. Liu, X. Zhang, W. Jiang, M. Wu, Z. Li, Comprehensive review of floc growth and structure using electrocoagulation: characterization, measurement, and influencing factors, *Chem. Eng. J.* 417 (2021) 129310–129334, <https://doi.org/10.1016/j.cej.2021.129310>.
- [51] Y. Zhu, Z. Qin, X. Shi, X. Ding, V.-D. Dao, Y. Li, Size-dependent activity modulation of supported Ni nanocatalysts for efficient solid-state hydrogen storage in magnesium, *Chem. Eng. Eng. J.* 498 (2024) 155285–155296, <https://doi.org/10.1016/j.cej.2024.155285>.
- [52] V.T. Nguyen, N.H. Pham, D.V. Papavassiliou, Aggregation of nanoparticles and morphology of aggregates in porous media with computations, *J. Colloid Interface Sci.* 650 (2023) 381–395, <https://doi.org/10.1016/j.jcis.2023.06.045>.
- [53] H. Xiang, D. Baudouin, F. Vogel, Metal oxide nanoparticles embedded in porous carbon for sulfur absorption under hydrothermal conditions, *Sci. Rep.* 13 (2023) 1–13, <https://doi.org/10.1038/s41598-023-36395-8>.
- [54] K. Mubeen, A. Irshad, A. Safeen, U. Aziz, K. Safeen, T. Ghani, K. Khan, Z. Ali, I. Ullah, A. Shah, Band structure tuning of ZnO/CuO composites for enhanced photocatalytic activity, *J. Saudi Chem. Soc.* 27 (2023) 101639–101652, <https://doi.org/10.1016/j.jscs.2023.101639>.
- [55] A. Nezamzadeh-Ejhieh, S. Hushmandrad, Solar photodecolorization of methylene blue by CuO/X zeolite as a heterogeneous catalyst, *Appl. Catal. A Gen.* 388 (2010) 149–159, <https://doi.org/10.1016/j.apcata.2010.08.042>.
- [56] P.G. Krishnan, P. Chandra Mishra, M.M. Naika, M. Gadewar, P.P. Ananthaswamy, S. Rao, S.R. Boselin Prabhu, K.V. Yatish, H.G. Nagendra, M. Moustafa, M. Al-Shehri, S.K. Jha, B. Lal, S.M. Stephen Santhakumari, Photocatalytic activity induced by metal nanoparticles synthesized by sustainable approaches: A comprehensive review, *Front. Chem.* 10 (2022) 917831–917852, <https://doi.org/10.3389/fchem.2022.917831>.
- [57] N.H. Mohd Kaus, A.F. Rithwan, R. Adnan, M.L. Ibrahim, S. Thongmee, S.F. Mohd Yusoff, Effective strategies, mechanisms, and photocatalytic efficiency of semiconductor nanomaterials incorporating rGO for environmental contaminant degradation, *Catalysts* 11 (2021) 302–327, <https://doi.org/10.3390/catal11030302>.
- [58] F. Kanwal, T. Javed, F. Hussain, M. Wasim, M. Batool, Enhanced dye photodegradation through ZnO and ZnO -based photocatalysts doped with selective transition metals: a review, *Environ. Technol. Rev.* 13 (2024) 754–793, <https://doi.org/10.1080/21622515.2024.2426725>.
- [59] A. Ranjbari, J. Yu, J. Kim, J. Kim, M. Park, K.-H. Kim, P.M. Heynderickx, Fundamental kinetic modeling of dye sensitization photocatalysis by oxygen vacancy enriched ZnO for the quantification of degradation by catalyst or dye sensitizer, *Appl. Surf. Sci.* 659 (2024) 159867–159932, <https://doi.org/10.1016/j.apsusc.2024.159867>.
- [60] S.-K. Chang, Q.-A. Abbasi, Z. Abbasi, F. Khushbakht, I. Ullah, F. Ur Rehman, M. Hafeez, Rapid pH-dependent photocatalytic degradation of methylene blue by CdS nanorods synthesized through hydrothermal process, *Arab. J. Chem.* 17 (2024) 105422–105430, <https://doi.org/10.1016/j.arabjc.2023.105422>.
- [61] M. Abdu, S. Tibebu, S. Babaee, A. Worku, T.A.M. Msagati, J.F. Nure, Optimization of photocatalytic degradation of Eriochrome black T from aqueous solution using TiO_2 -biochar composite, *Res. Eng. Des.* 25 (2025) 104036–104054, <https://doi.org/10.1016/j.rineng.2025.104036>.
- [62] M. Saberian, A. Nezamzadeh-Ejhieh, Synergistic photocatalytic degraded tetracycline upon supported CuO clinoptilolite nanoparticles, *Solid State Sci.* 147–161 (2024) 107381–107392, <https://doi.org/10.1016/j.solidstatesciences.2023.107381>.
- [63] M.A. Al-Gharibi, H.H. Kyaw, J.N. Al-Sabahi, M.T. Zar Myint, Z.A. Al-Sharji, M. Z. Al-Abri, Silver nanoparticles decorated zinc oxide nanorods supported catalyst for photocatalytic degradation of paracetamol, *Mater. Sci. Semicond.* 134 (2021) 105994–106004, <https://doi.org/10.1016/j.mss.2021.105994>.
- [64] S. Woo, H. Jung, Y. Yoon, Real-time UV/VIS spectroscopy to observe photocatalytic degradation, *Catalysts* 13 (2023) 683, <https://doi.org/10.3390/catal13040683>.
- [65] N. Jamal, A. Radhakrishnan, R. Raghavan, B. Bhaskaran, Efficient photocatalytic degradation of organic dye from aqueous solutions over zinc oxide incorporated nanocellulose under visible light irradiation, *Main Group Met. Chem.* 43 (2020) 84–91, <https://doi.org/10.1515/mgmc-2020-0009>.
- [66] A. Piscopo, D. Robert, J.V. Weber, Influence of pH and chloride anion on the photocatalytic degradation of organic compounds, *Appl. Catal. B Environ.* 35 (2001) 117–124, [https://doi.org/10.1016/S0926-3373\(01\)00244-2](https://doi.org/10.1016/S0926-3373(01)00244-2).
- [67] A. Farhat, J. Keller, S. Tait, J. Radjenovic, Assessment of the impact of chloride on the formation of chlorinated by-products in the presence and absence of electrochemically activated sulfate, *Chem. Eng. J.* 330 (2017) 1265–1271, <https://doi.org/10.1016/j.cej.2017.08.033>.
- [68] M.T. Thanh, T.V. Thien, P.D. Du, N.P. Hung, D.Q. Khieu, Iron doped zeolitic imidazolate framework (Fe-ZIF-8): synthesis and photocatalytic degradation of RDB dye in Fe-ZIF-8, *J. Porous. Mater.* 25 (2018) 857–869, <https://doi.org/10.1007/s10934-017-0498-7>.
- [69] B.K. Singh, Y. Kim, S. Kwon, K. Na, Synthesis of mesoporous zeolites and their opportunities in heterogeneous catalysis, *Catalysts* 11 (2021) 1541–1571, <https://doi.org/10.3390/catal11121541>.
- [70] W. Wang, F. Lin, B. Yan, Z. Cheng, G. Chen, M. Kuang, C. Yang, L. Hou, The role of seashell wastes in TiO_2 /seashell composites: photocatalytic degradation of methylene blue dye under sunlight, *Environ. Res.* 188 (2020) 109831–109865, <https://doi.org/10.1016/j.enrev.2020.109831>.
- [71] A.A. Mohammadi, B. Kamarehie, A. Jafari, N. Hosseingholizade, M. Ghaderpoori, M. Ahmadpour, M.Y.J. Baloch, Degradation of methylene blue in aqueous phase by homogenous and heterogeneous catalytic ozonation, *Res. Squ. 1* (2023) 1–13, <https://doi.org/10.21203/rs.3.rs-2642506/v1>.
- [72] R. Dhanabal, P.G. Priya, Optimization and photocatalytic degradation of crystal violet dye using Sr-ZnO /activated carbon nanoneedles, *Mater. Sci. Semicond. Process.* 192–203 (2025) 109481, <https://doi.org/10.1016/j.mss.2025.109481>.
- [73] A. Fernández-Pérez, T. Valdés-Solís, G. Marbán, Visible light spectroscopic analysis of methylene blue in water; the resonance virtual equilibrium hypothesis, *Dyes Pigments* 161 (2019) 448–487, <https://doi.org/10.1016/j.dyepig.2018.09.083>.

- [74] D. Cai, Y. Zhang, J. Li, D. Hu, M. Wang, G. Zhang, J. Yuan, Intermolecular interactions in mixed dye systems and the effects on dye wastewater treatment processes, RSC Adv. 14 (2024) 373–381, <https://doi.org/10.1039/D3RA01733H>.
- [75] H. Sajjad, A. Sajjad, R.T. Haya, M.M. Khan, M. Zia, Copper oxide nanoparticles: in vitro and in vivo toxicity, mechanisms of action and factors influencing their toxicology, Comp. Biochem. Physiol. C Toxicol. Pharmacol. 271 (2023) 109682–109693, <https://doi.org/10.1016/j.cbpc.2023.109682>.
- [76] Cytotoxic effects caused by functionalized carbon nanotube in murine macrophages, Cell. Physiol. Biochem. 56 (2022) 514–529, <https://doi.org/10.33594/000000573>.
- [77] Y. Li, X. Xia, Z. Niu, K. Wang, J. Liu, X., Li, hCeO₂@ Cu_{5.4}O nanoparticle alleviates inflammatory responses by regulating the CTSB–NLRP3 signaling pathway, Front. Immunol. 15 (2024) 1344098–1344109, <https://doi.org/10.3389/fimmu.2024.1344098>.
- [78] Z. Ci, H. Wang, J. Luo, C. Wei, J. Chen, D. Wang, Y. Zhou, Application of nanomaterials targeting immune cells in the treatment of chronic inflammation, IJN 19 (2024) 13925–13946, <https://doi.org/10.2147/IJN.S497590>.
- [79] S. Padmanaban, D. Pully, A.V. Samrot, V. Gosu, N. Sadashivam, I.-K. Park, K. Radhakrishnan, D.-K. Kim, Rising influence of nanotechnology in addressing oxidative stress-related liver disorders, Antioxidants 12 (2023) 1405–1430, <https://doi.org/10.3390/antiox12071405>.
- [80] A. Giannetto, T. Cappello, S. Oliva, V. Parrino, G. De Marco, S. Fasulo, A. Mauceri, M. Maisano, Copper oxide nanoparticles induce the transcriptional modulation of oxidative stress-related genes in *Arbacia lixula* embryos, Aquat. Toxicol. 201 (2018) 187–197, <https://doi.org/10.1016/j.aquatox.2018.06.010>.
- [81] S. Khan, A.A. Ansari, A.A. Khan, M. Abdulla, O. Al-Obaid, R. Ahmad, In vitro evaluation of cytotoxicity, possible alteration of apoptotic regulatory proteins, and antibacterial activity of synthesized copper oxide nanoparticles, Colloids Surf. B Biointerfaces 153 (2017) 320–326, <https://doi.org/10.1016/j.colsurfb.2017.03.005>.
- [82] L.M. Tolliver, N.J. Holl, F.Y.S. Hou, H.-J. Lee, M.H. Cambre, Y.-W. Huang, Differential cytotoxicity induced by transition metal oxide nanoparticles is a function of cell killing and suppression of cell proliferation, Int. J. Mol. Sci. 21 (2020) 1731–1748, <https://doi.org/10.3390/ijms21051731>.
- [83] L.M. Romero, D.A. Palacio, S. Esquivel, G.A. Sánchez- Sanhueza, M. Montaño, D. Rojas, A.F. Jaramillo, C. Medina, C. Montalba, M.F. Meléndrez, Contact antibacterial and biocompatible polymeric, composite with copper zeolite filler and copper oxide, nanoparticles: A step towards new raw materials for the biomedical industry, Polymer 315 (2024) 127795–127807, <https://doi.org/10.1016/j.polymer.2024.127795>.
- [84] A. Manke, L. Wang, Y. Rojanasakul, Mechanisms of nanoparticle-induced oxidative stress and toxicity, Biomed. Res. Int. 2013 (2013) 1–15, <https://doi.org/10.1155/2013/942916>.
- [85] M. Mrakovcic, M. Absenger, R. Riedl, C. Smole, E. Roblegg, L.F. Fröhlich, E. Fröhlich, Assessment of long-term effects of nanoparticles in a microcarrier cell culture system, PLoS One 8 (2013) e56791–e56801, <https://doi.org/10.1371/journal.pone.0056791>.
- [86] E. Fröhlich, C. Samberger, T. Kueznik, M. Absenger, E. Roblegg, A. Zimmer, T. R. Pieber, Cytotoxicity of nanoparticles independent from oxidative stress, J. Toxicol. Sci. 34 (2009) 363–375, <https://doi.org/10.2131/jts.34.363>.
- [87] P. Crosswhite, Z. Sun, Nitric oxide, oxidative stress and inflammation in pulmonary arterial hypertension, J. Hypertens. 28 (2010) 201–212, <https://doi.org/10.1097/HJH.0b013e328332bcd>.
- [88] F.C. Cadoná, M.F. Manica-Cattani, A.K. Machado, R.M. Oliveira, E. Ribas Da Silveira Flóres, C. Assmann, T.D. Algarve, I.B.M. Da Cruz, Genomodifier capacity assay: a non-cell test using dsDNA molecules to evaluate the genotoxic/genoprotective properties of chemical compounds, Anal. Methods 6 (2014) 8559–8568, <https://doi.org/10.1039/C4AY01709A>.
- [89] C. Angelé-Martínez, K.V.T. Nguyen, F.S. Ameer, J.N. Anker, J.L. Brumaghim, Reactive oxygen species generation by copper(II) oxide nanoparticles determined by DNA damage assays and EPR spectroscopy, Nanotoxicology 11 (2017) 278–288, <https://doi.org/10.1080/17435390.2017.1293750>.
- [90] A. Scattareggia Marchese, E. Destro, C. Boselli, F. Barbero, M. Malandrino, G. Cardeti, I. Fenoglio, L. Lanni, Inhibitory effect against *listeria monocytogenes* of carbon nanoparticles loaded with copper as precursors of food active packaging, Foods 11 (2022) 2941–2957, <https://doi.org/10.3390/foods11192941>.
- [91] E. Boone, L.G.M. Baas-Becking, Salt effecys on eggs and nauplii of *Atermia salina* L, J. Gen. Physiol. 14 (1931) 753–763, <https://doi.org/10.1085/jgp.14.6.753>.
- [92] L.M. Gaetke, H.S. Chow-Johnson, C.K. Chow, Copper: toxicological relevance and mechanisms, Arch. Toxicol. 88 (2014) 1929–1938, <https://doi.org/10.1007/s00204-014-1355-y>.